FABRICATION AND CHARACTERIZATION OF SUSPENDED GRAPHENE DEVICES

by

Abdülkadir Canatar

Submitted to the Graduate School of Engineering and Natural Sciences
in partial fulfillment of
the requirements for the degree of
Master of Science

Sabancı University
Spring 2016

FABRİCATİON AND CHARACTERİZATİON OF SUSPENDED GRAPHENE DEVİCES

APPROVED BY:

Assoc. Prof. Dr. Ismet Inönü Kaya
(Thesis Supervisor)

Prof. Dr. Cihan Saçlıoğlu

Asst. Prof. Dr. Cem Çelebi

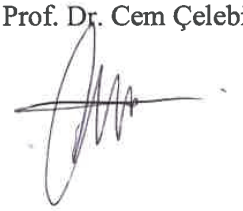

DATE OF APPROVAL: 11/July/2016

FABRICATION AND CHARACTERIZATION OF SUSPENDED GRAPHENE DEVICES

Abdülkadir Canatar

Physics, Master of Science Thesis, 2016

Thesis Supervisor: Assoc. Prof. Dr. İsmet İnönü Kaya

Abstract

Graphene as a two-dimensional conducting material has attracted enormous attention due to its relativistic nature and interesting physical properties. Although theoretical studies on graphene are quite successful and revealing many interesting results about Dirac-like condensed matter systems, experimental realizations of these predictions are very challenging. Due to the naturally occurring electron-hole puddles and impurities acquired during the fabrication, graphene devices merely show their true potential, i.e. strongly correlated physics at the Dirac point. In order to achieve an ultra-high quality graphene device with less impurity concentration and higher carrier mobility, graphene sheets are whether suspended or placed on an atomically flat hBN layer, both of which reduce electron-hole puddles and lead ultra-high mobility graphene samples.

This study introduces the techniques developed for fabricating ultra-clean, high mobility suspended monolayer graphene devices, which make Dirac point more accessible and produce high quality graphene samples. The fabrication and cleaning techniques (i.e. current annealing) leading devices with charge mobility values in excess of $10^6 cm^2/(V.s)$ will be presented and the data revealing the improvement in graphene quality after current annealing will be discussed.

ASKIDA GRAFEN AYGITLARININ ÜRETİMİ VE KARAKTERİZASYONU

Abdülkadir Canatar

Fizik, Master Tezi, 2016

Tez Danışmanı: Doç. Dr. İsmet İnönü Kaya

Özet

İki boyutlu iletken bir mazleme olarak grafen, rölativistik doğası ve ilginç fiziksel özellikleri dolayısıyla son zamanlarda oldukça ilgi çekmiştir. Grafen üzerine yapılan teorik çalışmaların oldukça başarılı ve bu çalışmaların Dirac-vari yoğun madde sistemlerinde bir çok ilginç sonuca varmasına rağmen, bu tahminlerin deneysel olarak gerçeklenmesi oldukça zorlayıcıdır. Doğal olarak meydana gelen elektron-boşluk birikintileri ve aygıtın üretimi sırasında ortaya çıkan kirlilikler, Dirac noktasındaki kuvvetle-ilintili fizik gibi grafenin gerçek potansiyelinin ortaya çıkmasını çoğu zaman engeller. Daha az kirlilik yoğunluğuna sahip ve yüksek taşıyıcı hareketliliğine sahip, üstün kaliteli grafen aygıtlarının elde edilebilmesi için grafen malzemesi ya askıda bırakılır ya da atomik seviyede düz olan hBN katmanlarının üzerine konulur. Bu iki yöntem de elektron-boşluk birikintilerini azaltır ve yüksek taşınımlı grafen aygıtlarının elde edilmesini sağlar.

Bu çalışmada, Dirac noktasını daha ulaşılabilir hale getiren ve yüksek kaliteli grafen örneklerinin üretilmesini olanak kılan, üstün temizlikte ve yüksek taşınımda askıda grafen aygıtlarının üretilmesi için geliştirilen teknikleri anlatılmaktadır. Tez boyunca yük taşınım değerleri $10^6 cm^2/(V.s)$'i aşan aygıtların üretimi ve temizlenmesi (akım tavlama) sunulacak ve akım tavlama sonrası grafen kalitesindeki artışı ortaya koyan veriler tartışılacaktır.

ACKNOWLEDGEMENTS

I would like to thank İsmet İnönü Kaya, my supervisor, for being a great teacher and encouraging research advisor. I started in his group 5 years ago, when I was a prep-school student at Sabancı University, and he always pushed and highly encouraged me to join to the research in any possible way, even I failed at the beginning. His great contribution to the development of my academic and personal identity is indisputable.

I would also like to thank Cenk Yanık who is a PhD student in our lab and my best friend. I have learned from him a lot, both in terms of research and life. Without him, most of our research and this thesis were not possible.

Finally, I would like to thank my family for their infinite support and all of my friends who made me enjoy my life.

Contents

List of Figures

Chapter 1

INTRODUCTION

1.1 Motivation

Graphene as a natural two-dimensional material has attracted tremendous attention in recent years and it is still studied extensively. The reason behind this interest is that graphene shows a Dirac-like dispersion at low energy excitations and therefore is the condensed matter analogue of the relativistic high-energy particles. Its excitations are called Dirac fermions and are effectively massless at low energies, which can exhibit relativistic phenomena like Klein tunnelling and Zitterbewegung [1, 5, 6]. Moreover, at Dirac point where the charge concentration in the material is very low, many interesting many-body phenomena can emerge and recently scientist managed to show very interesting phenomena like viscous behaviour of the charge carriers leading to non-local negative resistance [7, 8] and the breakdown of Wiedemann-Franz law which hints at the formation of a strongly-correlated Dirac fluid [9].

All of these exciting discoveries, however, require the fabrication of ultra-clean and impurity-free graphene devices in order to achieve the theoretical limit of graphene and make the Dirac point more accessible where the strongly-correlated physics gets more observable. In the experimental side of the graphene research, both fabrication and characterization techniques are getting more and more advanced and leading the ultimate purpose of achieving the perfect and reproducible graphene devices. This thesis is devoted to exploration of new fabrication techniques for the production of higher quality devices in order to make the interesting strongly-correlated physical phenomena in graphene more accessible.

1.2 Overview

In the next chapter of this thesis, we give an overview of the theory of the graphene physics by starting with the tight binding model for obtaining the low-energy band structure of graphene. Following that, magneto-transport properties of graphene are introduced by examining classical and quantum Hall effects in generic two-dimensional electron gases, and subsequently in graphene.

In the third chapter, fabrication of suspended monolayer graphene devices is thoroughly explained together with Raman analysis which provides an information about the layer number of the exfoliated graphene. This chapter starts with the exfoliation and identification of the graphene samples obtained from bulk graphene, and then continues with the chemical processes which are involved in the fabrication of suspended graphene devices.

The fourth and fifth chapter introduces the current annealing technique which is the most important step in the path of obtaining an ultra-high quality graphene. Firstly, current annealing is discussed in terms of its difficulties and the possible solutions. Secondly, a new technique developed in our group is explained through temperature simulations of the graphene devices, its utilization and outcomes. Finally, transport experiments carried out on these devices are introduced and discussed in terms of efficiency and device quality.

The last chapter concludes this thesis by discussing the results obtained from this research.

Chapter 2

ELECTRONIC PROPERTIES OF GRAPHENE AND QUANTUM TRANSPORT

In this chapter, graphene energy dispersion is derived by using the tight-binding model and its Hamiltonian is obtained in low-energy regime. First, lattice structure of graphene is shown and its lattice vectors are derived. Then using the tight-binding model, we show that at low energies, its electron wave functions obey Dirac Hamiltonian.

In the following section, classical and quantum Hall effects are introduced in order to understand the magneto-transport in graphene. Finally, anomalous QHE sequence in graphene is described and its implications are discussed.

2.1 Tight Binding Model of Graphene

Graphene is first isolated by Geim and Novoselov in 2004 although it was thought that 2D materials are mechanically unstable [5]. However, its theoretical prediction was made by Wallace in 1947, long before its first isolation [10]. In this section, we follow the tight-binding model approach by extracting its nearest-neighbor translation vectors and obtaining the Bloch wavefunctions in order to obtain the energy-momentum relation of graphene.

2.1.1 Lattice Structure

Graphene is a two-dimensional material with carbon atoms arranged in a hexagonal lattice. The unit cell of the hexagonal lattice consists of two carbon atoms with a separation of 1.42 Å and these carbon atoms are labeled as A and B lattice sites. Graphene lattice together with lattice a_1 and a_2 and nearest-neighbor δ_1, δ_2 and δ_3 translation vectors are

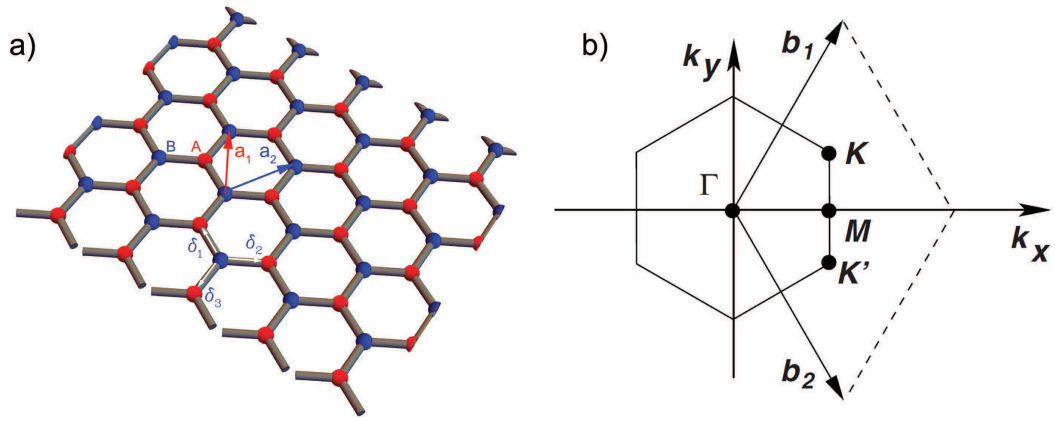

Figure 2.1: a) Graphene lattice illustrated with A and B sites and the lattice translation vectors a_1 and a_2. δ_1, δ_2, δ_3 are the translation vectors from one site to other. b) Reciprocal lattice of graphene illustrated with K and K' points and the Brillouin zone translation vectors b_1 and b_2 [1].

illustrated in Fig.2.1a. In Fig.2.1b, the corresponding Brillouin zone together with the reciprocal lattice translation operators are illustrated [1].

The real space lattice, nearest-neighbor and reciprocal lattice translation vectors are given by Equation 2.1 where $\vec{e_1}$ and $\vec{e_2}$ are the unit vectors x and y directions.

$$\begin{aligned}
\vec{a_1} &= \frac{a}{2}(3\vec{e_1} + \sqrt{3}\vec{e_2}), \vec{a_2} = \frac{a}{2}(3\vec{e_1} - \sqrt{3}\vec{e_2}) \\
\vec{\delta_1} &= \frac{a}{2}(\vec{e_1} + \sqrt{3}\vec{e_2}), \vec{\delta_2} = \frac{a}{2}(\vec{e_1} - \sqrt{3}\vec{e_2}), \vec{\delta_3} = -\frac{a}{2}\vec{e_1} \\
\vec{b_1} &= \frac{2\pi}{3a}(\vec{e_1} + \sqrt{3}\vec{e_2}), \vec{a_2} = \frac{2\pi}{3a}(\vec{e_1} - \sqrt{3}\vec{e_2})
\end{aligned} \tag{2.1}$$

2.1.2 Effective Low Energy Hamiltonian and Dispersion Relation

Tight binding model expresses the hopping terms in the Hamiltonian. In the graphene case, we consider the hopping possibilities from site A to site B which corresponds to nearest-neighbor hopping. One can also consider next nearest-neighbor hopping and so on. The generic Hamiltonian for such a system is given by:

$$\mathcal{H} = -t_1 \sum_{<i,j>} a_i^\dagger b_j - t_2 \sum_{<<i,j>>} a_i^\dagger a_j - t_3 \sum_{<<<i,j>>>} a_i^\dagger b_j + ... + h.c. \tag{2.2}$$

Here t_i parameters represent the strength of the hoppings and $< i, j >$ represents nearest-neighbour hopping, $<< i, j >>$ next-nearest-neighbour hopping and so on. Reported values from the numerical calculations for t_1, t_2 and t_3 are, respectively, 2.74,

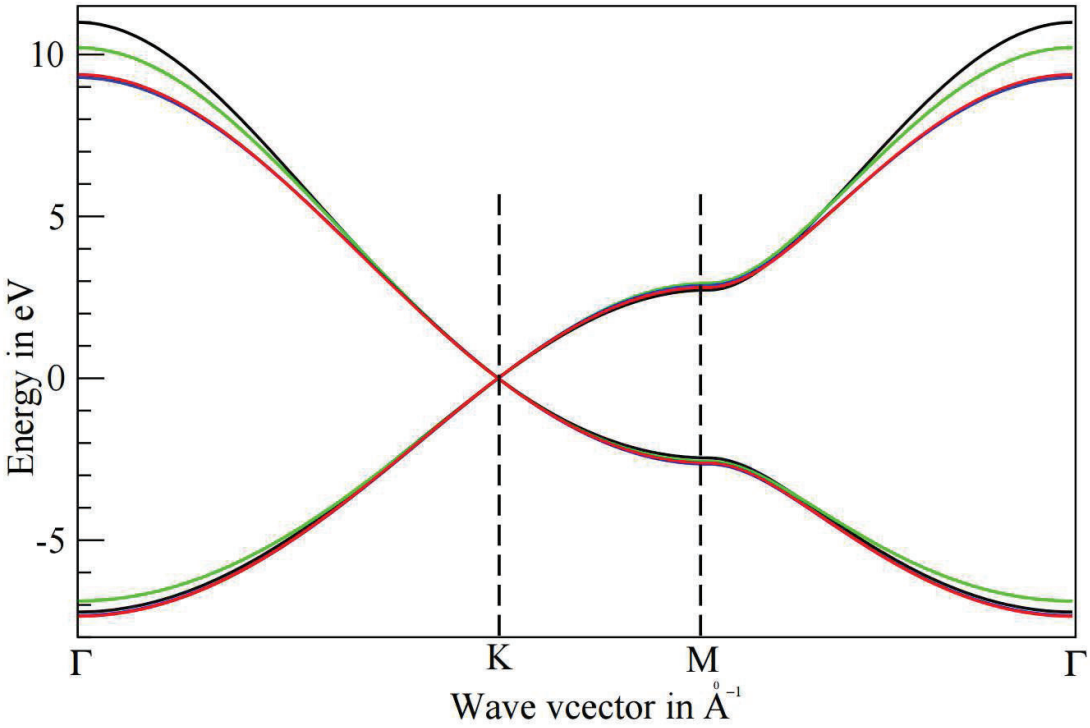

Figure 2.2: Graphene band diagram with three different Hamiltonian configurations. Green, blue and red curves correspond to Hamiltonians with only nearest-neighbor, 1^{st} and 2^{nd} nearest-neighbor and 1^{st}, 2^{nd} and 3^{rd} nearest-neighbor hopping, respectively [2].

0.07, 0.015 [2]. The differences in energy band diagram is shown in Fig.2.2. Since there is no significant change in the energy diagram, we only focus on nearest-neighbor hopping and ignore others for the sake of calculation simplicity.

Then our model with nearest-neighbor hopping is given by:

$$\mathcal{H} = -t_1 \sum_{<i,j>} {a_{\vec{r}_i}}^{\dagger} b_{\vec{r}_j} + {b_{\vec{r}_i}}^{\dagger} a_{\vec{r}_j} \tag{2.3}$$

where $a^{\dagger}_{\vec{r}_i}, a_{\vec{r}_i}, b^{\dagger}_{\vec{r}_i}, b_{\vec{r}_i}$ stand for the creation and annihilation operators of the electrons at the sublattices A and B which are located at the position $\vec{r}_i$. Since the summation is over the nearest-neighbors, we can explicitly write the Hamiltonian using the nearest-neighbor translation vectors introduced in Section 2.1.1.

$$\mathcal{H} = -t_1 \sum_i a^{\dagger}_{\vec{r}_i} b_{\vec{r}_i+\vec{\delta_1}} + a^{\dagger}_{\vec{r}_i} b_{\vec{r}_i+\vec{\delta_2}} + a^{\dagger}_{\vec{r}_i} b_{\vec{r}_i+\vec{\delta_3}} + h.c. \tag{2.4}$$

Now, we take the Fourier transform of these operators using the following convention:

$$
\begin{aligned}
a_k &= \frac{1}{\sqrt{N}} \sum_{\vec{r}} a_i e^{i\vec{k}.\vec{r}} \Rightarrow a_i = \frac{1}{\sqrt{N}} \sum_{k} a_k e^{-i\vec{k}.\vec{r}} \\
b_k &= \frac{1}{\sqrt{N}} \sum_{\vec{r}} b_i e^{i\vec{k}.\vec{r}} \Rightarrow b_i = \frac{1}{\sqrt{N}} \sum_{k} b_k e^{-i\vec{k}.\vec{r}}
\end{aligned}
\tag{2.5}
$$

where $\vec{r}$ sums are over all lattice sites. Now inserting these identities into the first term in Equation 2.4:

$$
\begin{aligned}
-t_1 \sum_i {a_{\vec{r}_i}}^\dagger b_{\vec{r}_i+\vec{\delta_1}} &= -\frac{t_1}{N} \sum_i \sum_k \sum_{k'} {a_k}^\dagger b_{k'} e^{i(\vec{k}-\vec{k'}).\vec{r_i}} e^{-i\vec{k'}.\vec{\delta_1}} \\
&= -\frac{t_1}{N} \sum_k \sum_{k'} {a_k}^\dagger b_{k'} e^{-i\vec{k'}.\vec{\delta_1}} N\delta_{kk'} \\
&= -t_1 \sum_k {a_k}^\dagger b_k e^{-i\vec{k}.\vec{\delta_1}}
\end{aligned}
\tag{2.6}
$$

Therefore, we will just replace each term in the Equation 2.4 with their Fourier partners with the additional phase factors:

$$
\mathcal{H} = -t_1 \sum_k {a_k}^\dagger b_k (e^{-i\vec{k}.\vec{\delta_1}} + e^{-i\vec{k}.\vec{\delta_2}} + e^{-i\vec{k}.\vec{\delta_3}}) + {b_k}^\dagger a_k (e^{i\vec{k}.\vec{\delta_1}} + e^{i\vec{k}.\vec{\delta_2}} + e^{i\vec{k}.\vec{\delta_3}}) \tag{2.7}
$$

This expression can be compactified by writing it in matrix form:

$$
\begin{aligned}
&\mathcal{H} = -t \sum_k \begin{pmatrix} {a_k}^\dagger & {b_k}^\dagger \end{pmatrix} \begin{pmatrix} 0 & \mathcal{H}_{ab} \\ \mathcal{H}_{ba} & 0 \end{pmatrix} \begin{pmatrix} a_k \\ b_k \end{pmatrix}, \\
&\mathcal{H}_{ab} = e^{-i\vec{k}.\vec{\delta_1}} + e^{-i\vec{k}.\vec{\delta_2}} + e^{-i\vec{k}.\vec{\delta_3}} \\
&\mathcal{H}_{ba} = e^{i\vec{k}.\vec{\delta_1}} + e^{i\vec{k}.\vec{\delta_2}} + e^{i\vec{k}.\vec{\delta_3}}
\end{aligned}
\tag{2.8}
$$

Energy eigenvalues are obtained by solving the eigenvalue equation for the matrix in Equation 2.8:

$$
\begin{aligned}
&\begin{vmatrix} -\epsilon & \mathcal{H}_{ab} \\ \mathcal{H}_{ba} & -\epsilon \end{vmatrix} = 0 \Rightarrow \epsilon^2 = \left|\mathcal{H}_{ab}\right|^2, \\
&\epsilon(k) = \pm \left|\mathcal{H}_{ab}\right| = \pm t \sqrt{3 + 2\cos(\sqrt{3}k_x a) + 4\cos(\frac{\sqrt{3}}{2}k_x a)\cos(\frac{3}{2}k_y a)}
\end{aligned}
\tag{2.9}
$$

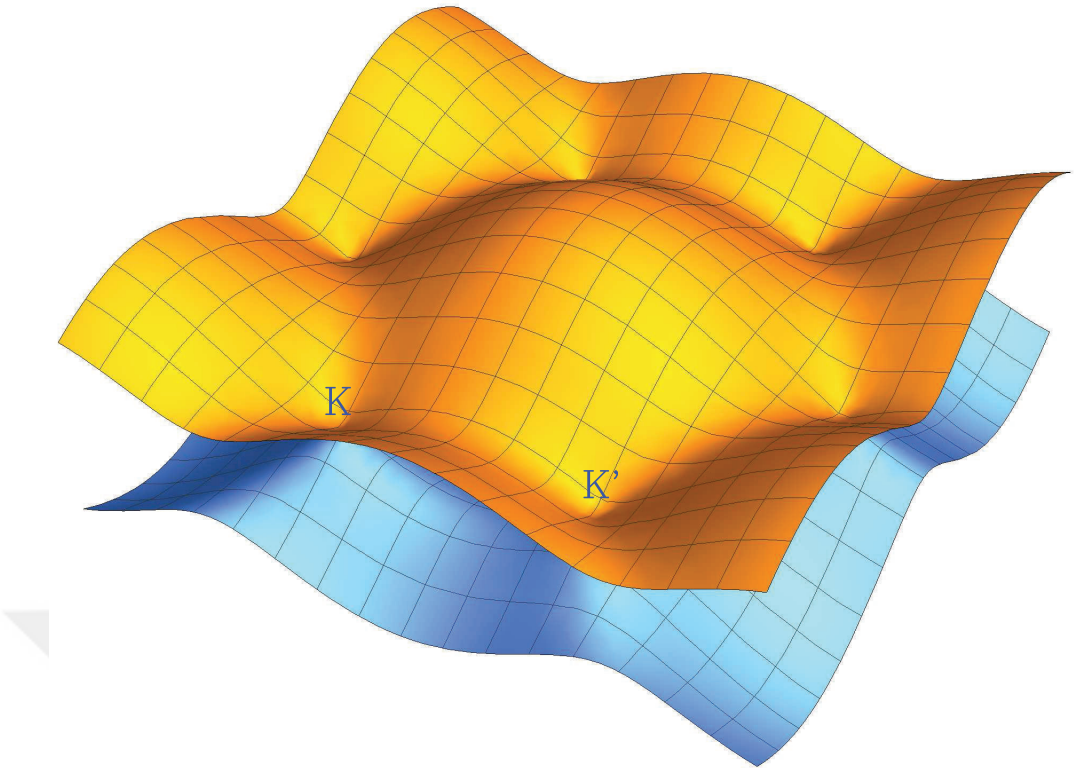

Figure 2.3: Graphene energy bands touching at $K = \frac{4\pi}{3\sqrt{3}a}$ and $K' = -\frac{4\pi}{3\sqrt{3}a}$.

The energy dispersion relation, therefore, is given in Equation 2.9. Energy dispersion relation is shown in Fig 2.3 where it is clearly seen that energy bands are touching each other at two distinct point in Brillouin zone, K and K'.

Having no band gap at two distinct points in Brillouin zone suggests to look into the low energy Hamiltonian of graphene. We can expand the energy expression given in Eq. 2.9 near the K and K' points:

$$\begin{aligned}
\epsilon(k) &= \pm \left| \mathcal{H}_{ab} \right| \\
&= \pm t \sqrt{3 + 2\cos\left(\sqrt{3}a\left(\frac{4\pi}{3\sqrt{3}a} + q_x\right)\right) + 4\cos\left(\frac{\sqrt{3}a}{2}\left(\frac{4\pi}{3\sqrt{3}a} + q_x\right)\right)\cos\left(\frac{3}{2}k_y a\right)} \\
&= \pm t \sqrt{3 + 2\cos\left(\frac{4\pi}{3} + \sqrt{3}aq_x\right) + 4\cos\left(\frac{2\pi}{3} + \frac{\sqrt{3}a}{2}q_x\right)\cos\left(\frac{3}{2}k_y a\right)} \\
&= \pm \frac{3}{2} ta \sqrt{q_x^2 + q_y^2} + \mathcal{O}(q^2)
\end{aligned} \tag{2.10}$$

Ignoring the order q^2 term in the last line in Equation 2.10, we can rewrite the Hamiltonian in the following form where v_F being the Fermi velocity which replaces speed of the light

c in quantum electrodynamics:

$$\mathcal{H} \approx \frac{3}{2}ta \begin{pmatrix} 0 & q_x - iq_y \\ q_x + iq_y & 0 \end{pmatrix} = v_F \vec{q}.\vec{\sigma} \tag{2.11}$$

Now we obtained the Dirac Hamiltonian as a low-energy model of graphene electrons. This result is one of the most striking outcome of the graphene physics which is a candidate for the test of high energy quantum electrodynamics in a usual condensed matter laboratory.

2.2 Magneto-transport in Graphene

In this section, electron transport in graphene under magnetic field is discussed. First, classical Hall effect is introduced and subsequently quantum Hall effect is discussed. Finally, quantum Hall effect and its anomalous sequence in graphene is introduced. In this section, David Tong's lecture notes are followed [11].

2.2.1 Classical Hall Effect

In order to understand quantum Hall effect clearly, we should study classical Hall effect first. We restrict the electrons to move only in two-dimensions and study their motion under an applied magnetic field perpendicular to the plane in which electrons moves. Due to the Lorentz force electrons move in a circle. Equation of motion for this problem is:

$$\begin{aligned} m\dot{\vec{v}} &= -e\vec{v} \times \vec{B} \\ m(\ddot{x}\hat{i} + \ddot{y}\hat{j}) &= -eB(\dot{y}\hat{i} - \dot{x}\hat{j}) \\ m\ddot{x} &= -eB\dot{y}, \quad m\ddot{y} = eB\dot{x} \end{aligned} \tag{2.12}$$

General solution for the last line in Equation 2.12 is given:

$$\begin{aligned} x(t) &= x_0 - r\sin(\omega_B + \phi), \\ y(t) &= y_0 - r\cos(\omega_B + \phi), \\ \omega_B &= \frac{eB}{m}. \end{aligned} \tag{2.13}$$

where (x_0, y_0) is the center of the cycle formed due to the magnetic field, r is the radius of the motion and ω_B is the cyclotron frequency. A schematic for this motion is shown in Figure 2.4a.

Now we extend our discussion by introducing an electric field and a frictional force emerging from the lattice scatterings. This model is called the Drude model. For this model, the equation of motion reads:

$$m\dot{\vec{v}} = -e\vec{E} - e\vec{v} \times \vec{B} - \frac{m\vec{v}}{\tau} \tag{2.14}$$

where τ is the scattering time and $\vec{E}$ is the electric field. For the sake of simplicity, we solve the equation for the steady-state which implies $\dot{\vec{v}} = 0$. Then we convert the equation to a readable form by using matrix notation and recalling the current density $\vec{J} = -ne\vec{v}$ where n is the electron density.

$$\begin{aligned}
&\vec{v} + \frac{e\tau}{m}\vec{v} \times \vec{B} = -\frac{e\tau}{m}\vec{E} \Rightarrow \vec{J} + \frac{e\tau}{m}\vec{J} \times \vec{B} = \frac{e^2 n\tau}{m}\vec{E}, \\
&\vec{J} = \begin{pmatrix} J_x \\ J_y \end{pmatrix} \quad \vec{J} \times \vec{B} = \begin{pmatrix} J_y B \\ -J_x B \end{pmatrix} \; and \quad \vec{E} = \begin{pmatrix} E_x \\ E_y \end{pmatrix}, \\
&\begin{pmatrix} J_x + \omega_B \tau J_y \\ J_y - \omega_B \tau J_x \end{pmatrix} = \frac{e^2 n\tau}{m} \begin{pmatrix} E_x \\ E_y \end{pmatrix}, \\
&\begin{pmatrix} 1 & \omega_B \tau \\ -\omega_B \tau & 1 \end{pmatrix} \vec{J} = \frac{e^2 n\tau}{m}\vec{E}
\end{aligned} \tag{2.15}$$

Inverting the last line in Equation 2.15, we obtain $\vec{J} = \sigma\vec{E}$ where σ is the conductivity tensor. If we explicitly invert this tensor, we obtain:

$$\begin{aligned}
\sigma &= \begin{pmatrix} \sigma_{xx} & \sigma_{xy} \\ -\sigma_{xy} & \sigma_{xx} \end{pmatrix} = \frac{\sigma_0}{1 + {\omega_B}^2 \tau} \begin{pmatrix} 1 & -\omega_B \tau \\ \omega_B \tau & 1 \end{pmatrix}, \\
\sigma_0 &= \frac{e^2 n\tau}{m}.
\end{aligned} \tag{2.16}$$

Here, we recover the usual Ohm's law in the absence of magnetic field which makes the conductivity tensor a scalar. But under the magnetic field conductivity deviates from the linear relationship between voltage and current since there Hall voltage is present

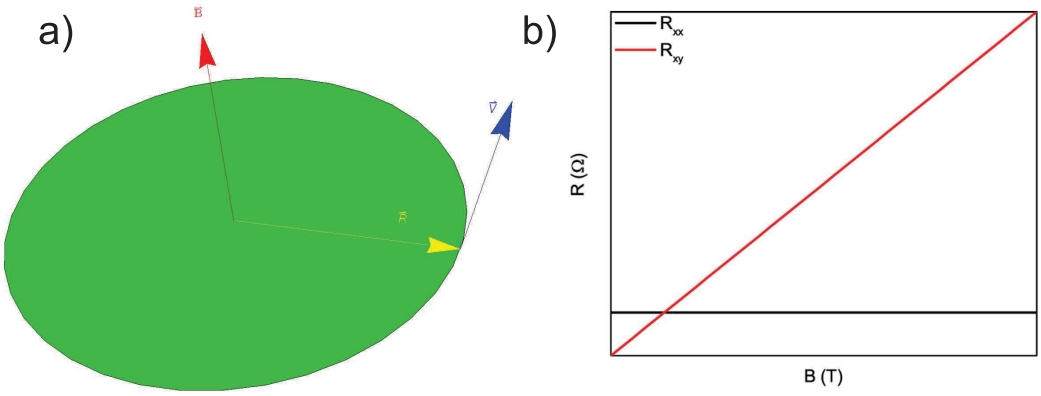

Figure 2.4: a) Electron orbits in classical Hall effect. $\vec{B}$ is perpendicular to the two-dimensional electron gas, $\vec{R}$ is the position vector of the electrons and $\vec{V}$ is the velocity vector of the particles. b) Behavior of Hall (R_{xy}) and longitudinal (R_{xx}) resistances under perpendicular magnetic field and in-plane electric field in x-direction.

together with the usual longitudinal voltage.

Next, we calculate resistivity out of conductivity. Since conductivity is a matrix, resistance defined as the inverse of conductivity is also going to be a matrix.

$$\rho = \sigma^{-1} = \begin{pmatrix} \rho_{xx} & \rho_{xy} \\ -\rho_{xy} & \rho_{xx} \end{pmatrix} = \frac{1}{\sigma_0} \begin{pmatrix} 1 & \omega_B \tau \\ -\omega_B \tau & 1 \end{pmatrix} \tag{2.17}$$

Here, Hall components of this tensor are $\pm\frac{\omega_B \tau}{\sigma_0}$ which is equal to $\pm\frac{B}{en}$. This tells us that Hall resistivity is independent of τ which changes from sample to sample and is related to the dirt on the sample which scatters the charge carriers. Therefore, Hall resistivity is something fundamental which only depends on the magnetic field and the carrier concentration.

Further, resistance which is different from the resistivity and depends on the geometry of the sample, as well. Hall resistance is defined as the division of the voltage drop in the direction perpendicular to the current flow and the current passing through the device. Assuming the current is flowing in the x-direction and the device has the width of L in the y-direction, voltage drop across the y-direction will be LE_y and current flowing through x-direction is the current density times the cross section current passing through, $I_x = LJ_x$:

$$R_{xy} = \frac{V_y}{I_x} = \frac{LE_y}{LJ_x} = -\rho_{xy} \tag{2.18}$$

Therefore, Hall resistance and Hall resistivity are the same quantities. Since resistance is what is measured in experiments, we can predict the change in Hall and (assuming width and length are the same) longitudinal resistance versus magnetic field as shown in Equation 2.19. A comparative sketch of the resistance change versus magnetic field in an experimental setup is shown in Figure 2.4b.

$$R_{xy} = \rho_{xy} = \frac{B}{en}, \quad R_{xy} = \frac{L}{W}\rho_{xx} = \frac{m}{ne^2\tau} \tag{2.19}$$

2.2.2 Quantum Hall Effect

As the semiconductor technology advances, electrons can be got confined in narrower regions and the electron gas becomes more and more two-dimensional. In 1980, von Klitzing measured a Si-MOSFET sample under high magnetic fields and low temperatures. What he found was the quantization of the Hall resistance at certain values over a considerable range of magnetic field [3]. These certain resistances are given in Equation 2.20 and the resistances are shown in Figure 2.5.

$$\rho_{xy} = \frac{e^2}{h}\nu, \quad \nu = 1, 2, 3, ... \tag{2.20}$$

This effect can be explained by the quantized Landau levels emerging from the solution of Schrödinger equation under magnetic field. When a Landau level is completely filled up and while chemical potential is being swept until the next Landau level, all the electrons stay in the Landau level they filled over a certain range, which corresponds to the plateaus seen in the Figure 2.5a. When they start to fill up the next Landau level, there is a resistance peak in the longitudinal resistance and deviation from the quantized Hall resistance.

First, we start with the Schrödinger equation with the gauge invariant Hamiltonian. For the vector potential, we use Landau gauge where $\vec{A} = Bx\hat{y}$ for the constant magnetic field $\vec{B} = B\hat{z}$.

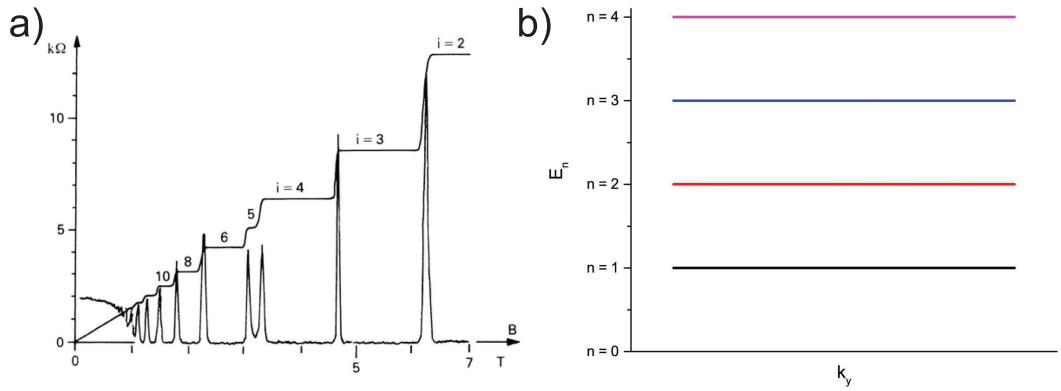

Figure 2.5: a) Hall and longitudinal resistance versus magnetic field during the Quantum Hall Effect [3]. b) Highly degenerate Landau levels.

$$\begin{aligned}\mathcal{H} = \frac{1}{2m}(\vec{p} + \frac{e}{c}\vec{A})^2 &= \frac{1}{2m}\left[p_x\hat{x} + \left(p_y + \frac{eB}{c}x\right)\hat{y}\right]^2 \\ &= \frac{{p_x}^2}{2m} + \frac{1}{2m}\left(p_y + \frac{eB}{c}x\right)^2\end{aligned} \tag{2.21}$$

Since p_y commutes with this Hamiltonian, we can replace it by its eigenvalue $\hbar k_y$.

$$\begin{aligned}\mathcal{H} =& \frac{{p_x}^2}{2m} + \frac{1}{2m}\left(\hbar k_y + \frac{eB}{c}x\right)^2 = \frac{{p_x}^2}{2m} + \frac{1}{2m}\left(\frac{eB}{c}\right)^2\left(x + \frac{\hbar c k_y}{eB}\right)^2 \\ \Rightarrow \mathcal{H} =& \frac{{p_x}^2}{2m} + \frac{1}{2}m{\omega_0}^2\big(x + x_c\big)^2, \quad \omega_0 = \frac{eB}{mc}, \quad x_c = \frac{\hbar k_y}{m\omega_0}\end{aligned} \tag{2.22}$$

Last line in Equation 2.22 indicates that the energy levels for this Hamiltonian is exactly the same to that of quantum harmonic oscillator. The resulting Landau levels are given in Equation 2.23. However, these energy levels are only dependent on magnetic field and not dependent on k_y which means there is degeneracy in the Landau levels. This degeneracy is proportional to the area of the sample which is quite large. Energy-momentum relation for the Landau levels are shown in Figure 2.5b.

$$E_n = \hbar\omega_0\left(n + \frac{1}{2}\right) \tag{2.23}$$

2.2.3 Anomalous QHE Sequence in Graphene

In graphene, however, charge carriers obey low-energy massless Dirac equation but not the Schrödinger equation. Therefore, we need to recalculate the energy eigenenergies of the Dirac equation under magnetic field which is included in the theory by adding the vector potential $\vec{A}$. We start with the Dirac Hamiltonian for graphene derived in this chapter. In this subsection, we work in the units where $c = \hbar = 1$.

$$\mathcal{H} = v_F \vec{p}.\vec{\sigma} = v_F \begin{pmatrix} 0 & p_x - ip_y \\ p_x + ip_y & 0 \end{pmatrix} \tag{2.24}$$

Now, we solve for the eigenenergies of this Hamiltonian:

$$\begin{aligned} v_F \begin{pmatrix} 0 & p_x - ip_y \\ p_x + ip_y & 0 \end{pmatrix} \begin{pmatrix} \chi_1 \\ \chi_2 \end{pmatrix} &= E \begin{pmatrix} \chi_1 \\ \chi_2 \end{pmatrix} \\ \Rightarrow (p_x - ip_y)\chi_2 = \frac{E}{v_F}\chi_1 \;\&\; (p_x + ip_y)\chi_1 &= \frac{E}{v_F}\chi_2 \end{aligned} \tag{2.25}$$

Using these coupled equations and solving for one of them:

$$\begin{aligned} \frac{E^2}{{v_F}^2}\chi_1 &= (p_x - ip_y)(p_x + ip_y)\chi_1 \\ &= \left[{p_x}^2 + {p_y}^2 + i[p_x, p_y]\right]\chi_1 \end{aligned} \tag{2.26}$$

Since, gauge transformation for momentum is $\vec{p} \rightarrow \vec{p} - e\vec{A}$, and we fix the gauge by using Landau gauge which is $\vec{A} = eBx\hat{e_2}$,

$$\left[{p_x}^2 + {p_y}^2 + i[p_x, p_y]\right]\chi_1 = \left[{p_x}^2 + (p_y - eBx)^2 + i[p_x, (p_y - eBx)]\right]\chi_1 \tag{2.27}$$

Since, the commutator $[p_x, p_y] = 0$ and $[x, p_x] = i$, we obtain:

$$\begin{aligned} \frac{E^2}{{v_F}^2}\chi_1 &= \left[{p_x}^2 + (p_y - eBx)^2 - eB\right]\chi_1 \\ \left(\frac{E^2}{{v_F}^2} + eB\right)\chi_1 &= \left[{p_x}^2 + (p_y - eBx)^2\right]\chi_1 \end{aligned} \tag{2.28}$$

Again, we will make this expression look like usual quantum harmonic oscillator as we did before:

$$\begin{aligned}\frac{\left(\frac{E^2}{{v_F}^2}+eB\right)}{2m}\chi_1 &= \left[\frac{{p_x}^2}{2m}+\frac{1}{2m}(p_y-eBx)^2]\right]\chi_1 \\ &= \left[\frac{{p_x}^2}{2m}+\frac{\tilde{k}^2}{2}(x-x_0)^2]\right]\chi_1\end{aligned} \tag{2.29}$$

where we introduced $\tilde{k}=e^2B^2/m$ and $x_0=k_y/eB$. Now we convert the Dirac equation into a quantum harmonic oscillator which is shifted by x_0. Therefore the energy eigenvalues are:

$$\epsilon_n=\omega_0\left(n+\frac{1}{2}\right),\quad \omega_0=\sqrt{\frac{\tilde{k}}{m}}=\frac{eB}{m} \tag{2.30}$$

Comparing the left-hand side of Equation 2.29 and Equation 2.30, we obtain the energy eigenvalues in Equation 2.31.

$$\frac{\left(\frac{E^2}{{v_F}^2}+eB\right)}{2m}=\frac{eB}{m}\left(n+\frac{1}{2}\right),\ \Rightarrow\ E=\pm\sqrt{2eBn{v_F}^2},\ n=1,2,3,... \tag{2.31}$$

While Landau levels are linear in energy index in usual QHE, in Dirac theory, they are proportional to the square root of n. This property of Dirac theory allows the index 0, as well, which is called $n=0$ Landau level.

In experimental studies, graphene shows an anomalous sequence of quantum Hall effect such that the conductance quantization indexes go like $\nu=2,6,10,...=4(n{+}1/2)$. Normally, one would expect the quantization sequence $\nu=4,8,...=4n$, where the factor of 4 accounts for spin and valley degeneracy in graphene. But, this relation is solved by Gusynin and Sharapov in 2005 by claiming that the 0^{th} Landau level's degeneracy is half of the higher Landau level's degeneracy [12]. Therefore, the $1/2$ in the sequence $\nu=2,6,10,...=4(n+1/2)$ accounts for this anomaly of 2+1D Dirac theories. Figure 2.6 shows a typical monolayer graphene Hall effect sequence [4].

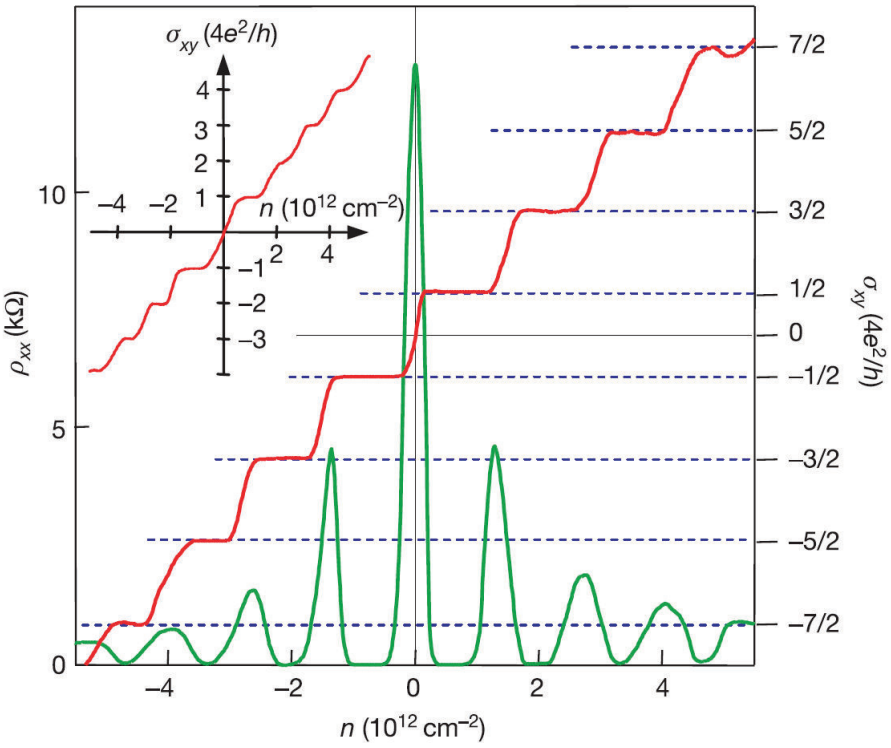

Figure 2.6: Quantum Hall effect in graphene is shown. Under magnetic field, electron density is swept with gate voltage. Graphene's anomalous quantum Hall sequence $\nu = 2, 6, 10, ... = 4(n + 1/2)$ is shown in the right axis. [4]

Chapter 3

FABRICATION AND CHARACTERIZATION OF SUSPENDED GRAPHENE

In this chapter, we explain the fabrication of suspended graphene devices and their characterizations, in detail. In the first section, exfoliation of graphene from Kish graphite and its Raman characterization are introduced. In the second section, fabrication steps of the device on the exfoliated graphene are illustrated. In this section, contact designs, E-Beam lithography and etching steps are explained.

3.1 Preparation of the Substrates and Exfoliation of Graphene

First, we start with preparing the SiO_x substrates for easing the E-Beam process and cleanliness. We use commercially available 4" silicon wafers which consist of highly-doped silicon with a thickness of 500 μm and silicon oxide grown on it with a thickness of 285 nm. These wafers are first exposed by E-Beam and coated with chromium and gold in order to create an array of numbers and markers which make locating the graphene found under the microscope much easier and are needed for the E-Beam alignment. E-Beam procedure is later explained in detail. Figure 3.1a shows a picture of commercially available Si wafers and 3.1b shows the markers and numbers patterned on a wafer.

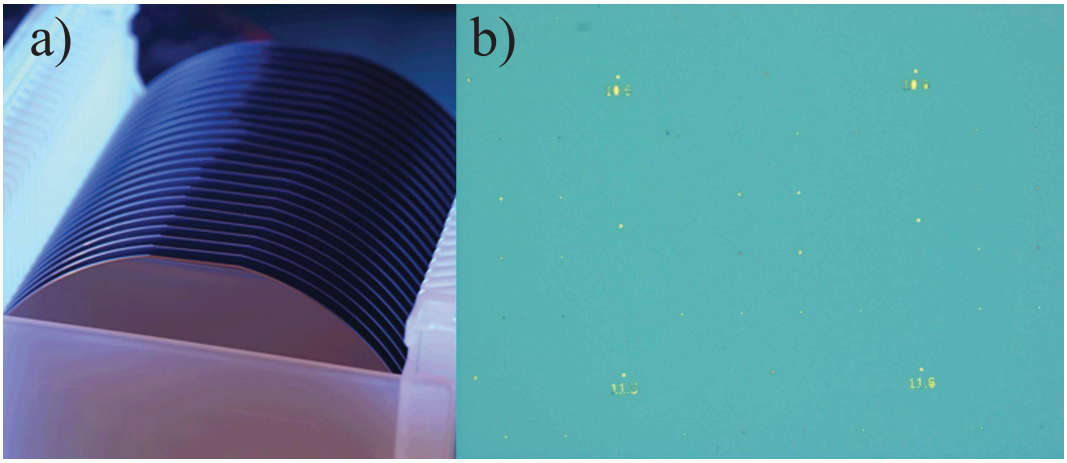

Figure 3.1: a) Commercially available Si wafers with 285 nm SiO_x grown on it. b) Markers and numbering are patterned and metal coated on the wafer for the E-Beam lithography.

After these steps, wafer is diced into little squares with dimensions $1mm \times 1mm$. Then, these diced substrates are dipped into the piranha solution consisting of 3:1 H_2SO_4 : H_2O_2 which removes all the organic residues and dirt on the wafer. Then optionally, we make oxygen plasma with an Oxford Reactive Ion Etching (RIE) system to the wafer to make sure of the cleanliness of the substrates. In Chapter 5, in fact, we realize that the latter step is the most crucial step for the successful suspension of graphene devices.

Next, we use the famous mechanical cleavage technique for obtaining graphene sheets to fabricate devices on it. This technique is first introduced to the literature by A. Geim and K. Novoselov in 2004, and it led them to win the Nobel Prize in 2010 for the discovery of graphene [5]. Using a scotch tape and by sticking the tape with itself, Kish graphite is divided into small and thin pieces and graphite is completely made cover the whole tape. This process keeps continue until graphite is homogeneously covered on the tape. Then, tape is sticked on the previously prepared clean SiO_x substrates and pressure is applied on the substrates, then the tape is slowly taken away. Resulting substrate is investigated under an optical microscope since graphene is identifiable by the contrast due to the oxide underneath [5]. When graphene sheets are identified, their positions are saved and the microscope images under several magnifications are taken in order to make a design on it with a layout software for E-Beam lithography. Figure 3.2a shows the mechanical exfoliation procedure and 3.2b shows a graphene sheet identified under the optical microscope.

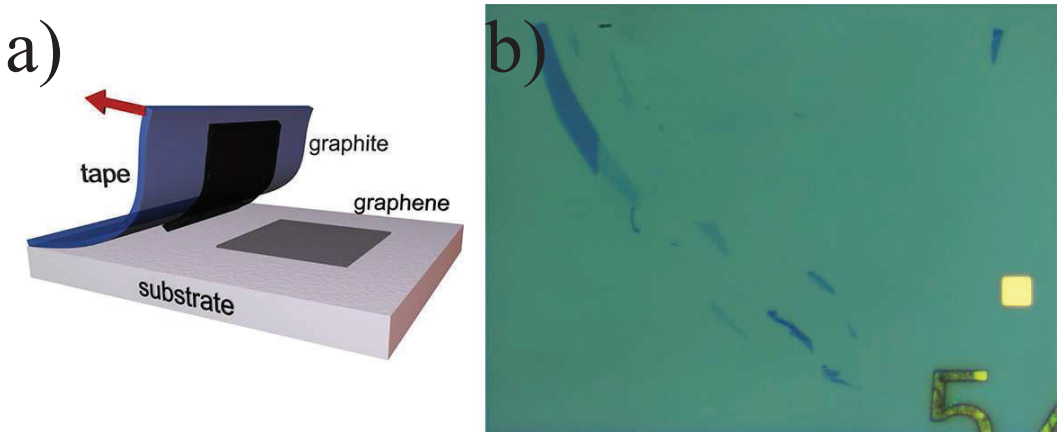

Figure 3.2: a) Mechanical cleavage of graphene demonstrated. b) A graphene sheet produced using the mechanical exfoliation technique.

Subsequently, identified graphene sheets are confirmed with Raman spectroscopy, since sometimes, graphene sheets looking monolayer at first may turn out to be bi- or multilayer graphene layers. The principle behind the Raman spectorscopy is the well-known Raman scattering where lattice vibrations change the wavelength of the light shining on the chemical structure. Acquiring the scattered light, spectroscope can identify the signatures of the molecules sitting on the substrate [13]. In Figure 3.3a, the Renishaw's Raman spectroscope that we use for our research is shown. Graphene also has certain signatures of being mono- or multilayer. Graphene has two significant peaks under Raman spectroscopy which are G band at around 1582 cm^{-1} coming from the first order Raman generation and G' band at around 2700 cm^{-1} stemming from the second order Raman generation. There is also disorder band 2D around at 1350 cm^{-1} which is self-explaining. If the graphene is monolayer, then the G'/G ratio almost approaches to 2, but otherwise, it is around 1 or less [14]. Figure 3.3b, shows the Raman spectroscopy of the graphene shown in Figure 3.2b.

After identifying a suitable graphene for the suspended graphene device fabrication, we start the device fabrication. We usually choose graphene pieces which are very narrow ($\sim 1\mu m$) and long ($\sim 10-15\mu m$). These pieces are the perfect fit for the suspended graphene devices since it is easier to etch underneath since it is narrow, and it is convenient to make designs which have multiple devices on one graphene piece. One can also etch a large piece of graphene with RIE to give it a suitable shape for the fabrication, but it is more convenient to use a naturally rectangular shaped graphene since we eliminate the possibility of dangling bonds and undesired edge effects arising when the graphene is

etched. For a demonstration, the graphene shown in Figure 3.2b is very suitable for the fabrication and experiments.

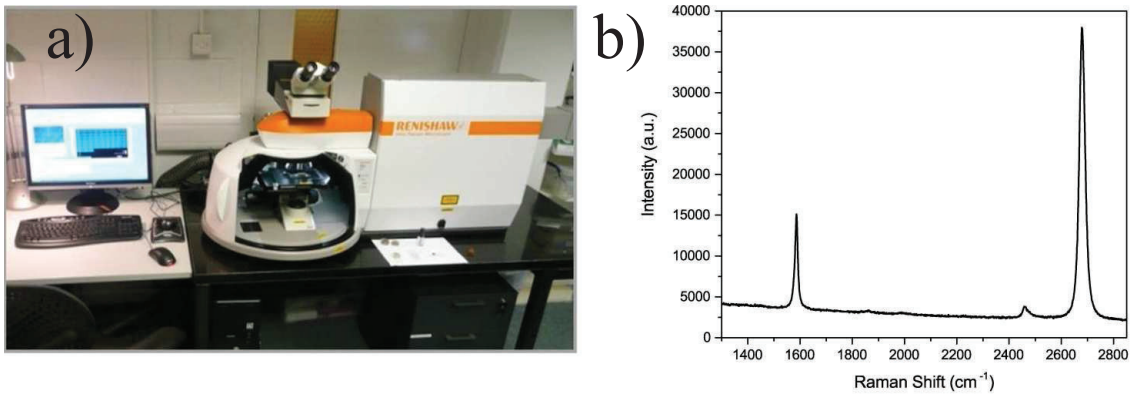

Figure 3.3: a) Renishaw Raman Spectroscopy instrument. b) Raman spectrum of the graphene in Fig. 3.2.

3.2 Fabrication of Graphene Devices

After identifying a suitable graphene for the suspended graphene device fabrication, we start the fabrication process. In this section, first we show how to make contact designs on the identified graphene sheets on the computer software LayoutEditor.

Then, we show how to import the designs to the E-Beam lithography system Vistec EBPG5000+ and how to utilize the E-Beam lithography to pattern our samples to put the contacts on the graphene.

Finally, we introduce the SiO_x etching with HF in order to suspend the graphene sheet in air while clamping it with the metal contacts.

3.2.1 Contact Design

In order to measure the graphene device electrically and hold the suspended sheet mechanically, we need to put metal on the edges of the graphene. After identifying the graphene sheets which are processed, we take their optical images in 5x, 10x, 20x 50x, 100x magnifications and import these images to LayoutEditor software. Using the previously evaporated metal markers and numbering, we align the sample images on a previously prepared contact design. Since the images are placed by considering the markers which are later used in aligning the real sample in the E-Beam lithography system, designs can be made directly on these images. Contact designs are shown in Figure 3.4a, which

have dimensions of $1900\mu m \times 1900\mu m$. Figure 3.4b shows the layout after aligning the sample images in the contact design.

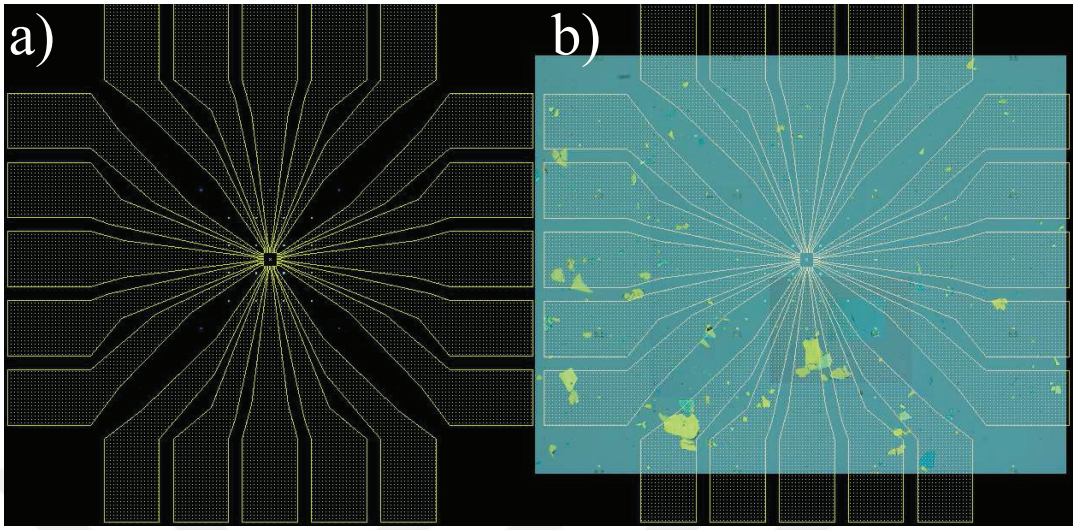

Figure 3.4: a) Contact design for the graphene devices. b) Contact design after the alignment of the images.

Contact designs are made according to some rules developed for effective annealing and sustaining a good mechanical stability to the suspended device. These rules are described in Chapter 4 in detail. Contact design made for the graphene in Figure 3.2b using LayoutEditor software is shown in Figure 3.5a and 3.5b.

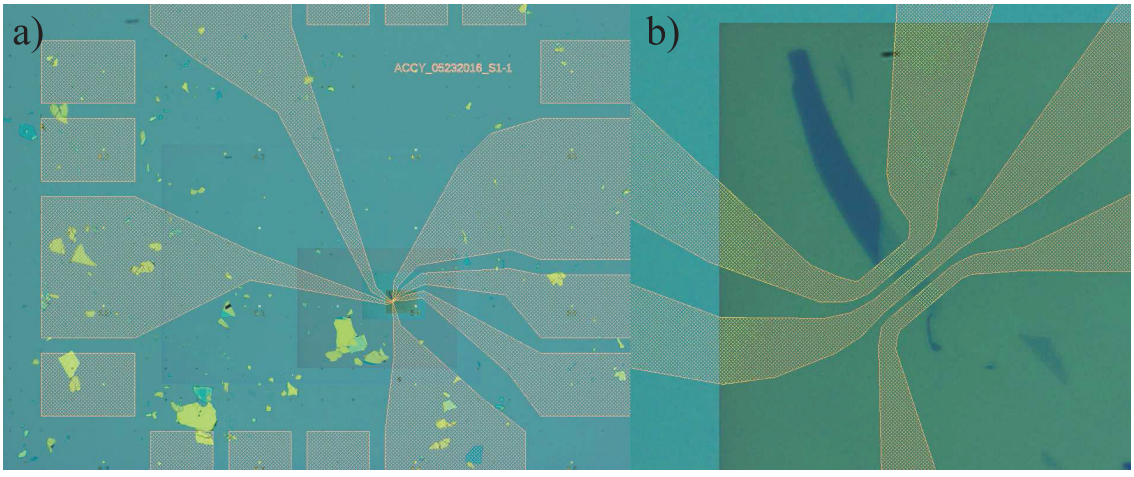

Figure 3.5: a) Contact design made on the sample shown in Figure 3.2b. b) A closer look at the contact design.

3.2.2 E-Beam Lithography and Metal Evaporation

In this subsection, we describe E-Beam lithography and its step. In order to evaporate metal on these highlighted areas in Figure 3.5, we coat the sample with a special material called resist, which changes its chemical structure when electron beams hit on it with a certain dose. In E-Beam lithography, we only expose these highlighted areas on the resist coated samples. After this, we immerse the exposed samples into a special liquid called developer which only resolves the areas where the chemical structure of the coated material is changed. This way, we open these exposed areas in order to evaporate metal on it. After evaporating the metal over the whole sample, we put the sample into acetone to remove the unexposed resist which removes the metal on it, as well. Therefore, metal is only coated on the exposed areas. This process is called lift-off. All these process are summarized in Figure 3.6a. Now, we explain the steps in detail.

After the design, we coat the sample with PMMA which is an E-Beam resist. First, we coat the sample with MMA EL11 which is a low-mass co-polymer, with a thickness of 400 - 450 nm with spin coater. Then, we coat 950 PMMA A2 which is a high-mass polymer. This process is called bilayer process which serves for easing the lift-off process. After exposing the sample and immersing the sample to developer, bottom layer MMA EL11 resolves more than the top layer PMMA A2 since MMA EL11 is a low-mass material.

Then, we place the sample into the E-Beam system. In the software of E-Beam lithography, we choose the dose with which the sample is exposed. For our process, we use $650\mu C/cm^2$ dose at 100 keV. Automatic software of the E-Beam system eases the patterning a lot, and we can quickly expose the samples.

After exposing the sample, we immerse our samples to the developer solution which consists of isopropanol and methyl isobutyl ketone with 3:1 ratio for 1 minute. After this process we obtain a structure which is shown in Figure 3.6b [15].

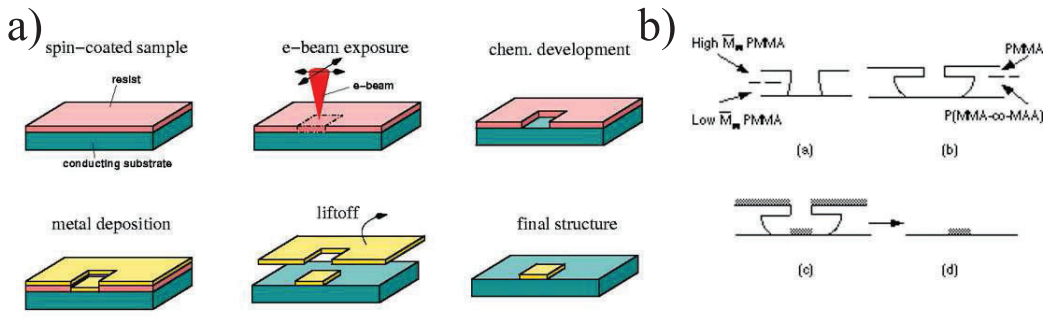

Figure 3.6: a) A schematic for E-Beam process, metal evaporation and lift-off. b) A closer look at the resist profile which eases lift-off.

Developed samples are loaded into a metal evaporator which is taken into low vacuum around $10^{-6} Torr$. Then, we evaporate 2 nm chromium and 100 nm gold by passing huge currents through the metals which are sitting on tungsten boats and baskets. Thickness of the evaporated metal is monitored by quartz crystal detectors.

Finally, we take out the samples and immerse them to acetone which solves PMMA. We usually wait overnight to have a clean and successful lift-off but it is not a must.

In Figure 3.7, fabrication process of the graphene device shown in Figure 3.2 is shown.

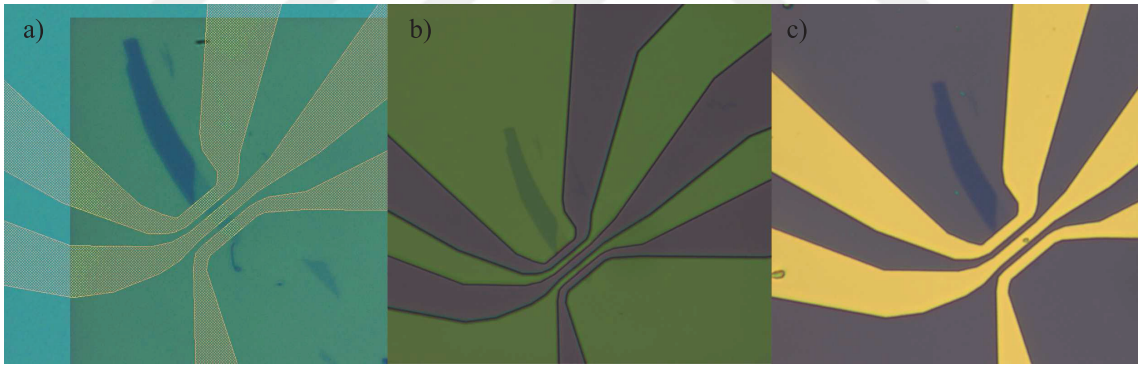

Figure 3.7: a) Contact design of the graphene design. b) Image after E-Beam lithography and development. Green regions are coated with resist and purple regions are developed. c) After metal deposition and lift-off.

3.2.3 Substrate Etching

After metal evaporation, we etch the SiO_x underneath the graphene for the suspension. We use 7:1 buffered oxide etch (BOE) which contains 7:1 volume ratio of 40% NH_4F in water and 49% HF in water. This etchant is vastly used in microelectronics industry and offers a very controlled etching processes with a rate of 1.2 nm/s. We usually etch the 200 nm of SiO_x under the graphene. Therefore, we immerse our samples into BOE for

2.45 minutes, and immediately after, put it into distilled water to stop the etching process. Then, we put the sample into hot isopropanol (IPA) which has a lower surface tension. After taking out from IPA, we dry the sample by nitrogen very slowly in order to prevent the collapse of the graphene. In figure 3.8a shows an image of the graphene device shown in Figure 3.7 after BOE etching. This device is not successfully etched and it is visible since there is a contrast with the substrate underneath. If it was completely suspended, nothing should be observed between the contacts since graphene is very transparent and absorbs only 2.3% precent of the light [16]. In figure 3.8b, an image of a successfully etched graphene device is shown. Graphene is barely seen on the metal contacts by changing the contrast and microscope aperture. The reason of the unsuccessful etching and its solution are discussed in Chapter 5 in detail.

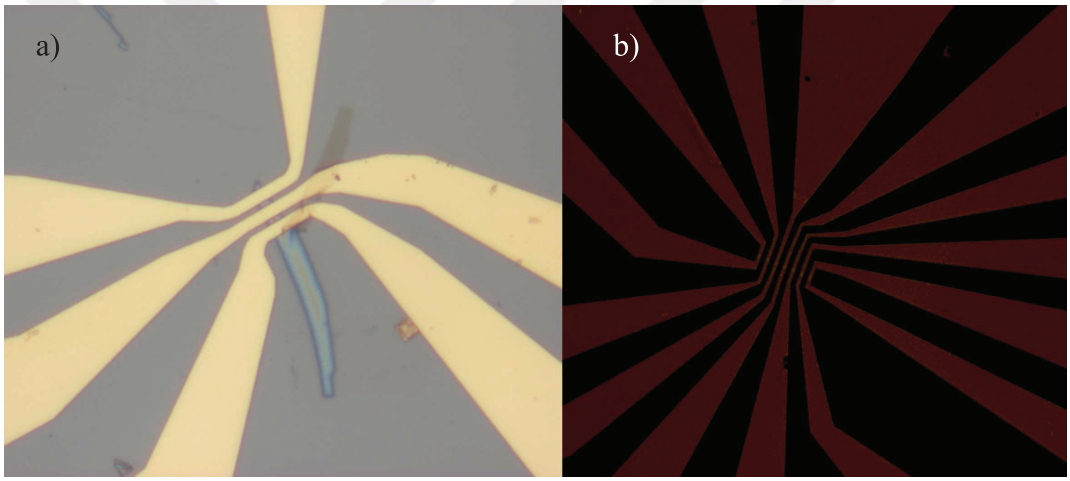

Figure 3.8: a) Image of an unsuccessful etching. Graphene can be seen between the metal probes. b) Image of a successfully etched sample. Graphene can be only seen on the metal probes by changing the contrast and microscope aperture.

Finally, we wire bond these samples to a chip carrier by using a Kulicke & Soffa wire bonder in order to load the samples into the cryostat for carrying out the experiments. Figure 3.9 shows the chip carrier with 20 pins with a device bonded.

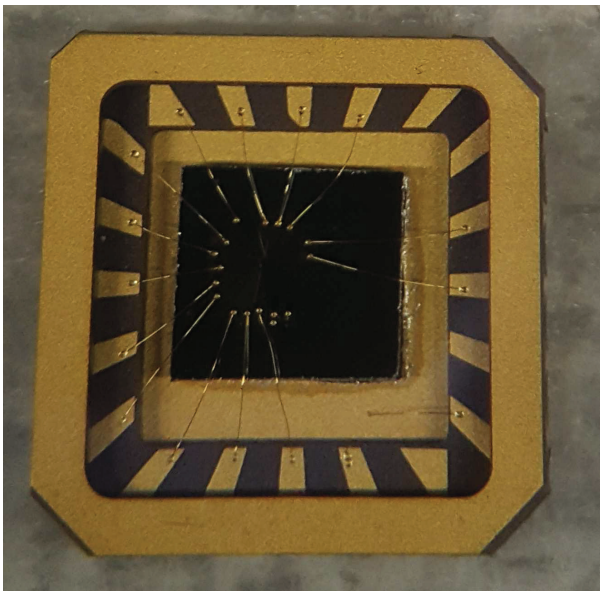

Figure 3.9: Image of a chip carrier with a graphene device bonded.

Chapter 4

CURRENT ANNEALING OF SUSPENDED GRAPHENE

Current annealing and cleaning of the suspended monolayer graphene devices are the main purpose of this thesis. In this chapter, the need for current annealing is explained and other possible solutions for the cleaning of graphene devices are introduced. In the first section, current annealing in the current literature is introduced and discussed.

In the subsequent section, our current annealing technique with split contacts are presented and its advantages are discussed. Temperature simulations of these split contact designs are shown and argued in terms of efficiency. Then, an automatic annealing software developed by our group in order to increase the yield of the annealing process and keep track of the significant changes in the graphene transport during the annealing is introduced. Finally, results are shared together with a broad discussion of our new technique.

4.1 Difficulties in Current Annealing

In order to remove disorders and impurities on graphene, researches tried $H_2 - Ar$ annealing around $200°C$ for the graphene samples on SiO_x [17]. With this technique, Morozov et.al. were able to reach high quality graphene devices whose carrier mobilities can exceed $200.000\ cm^2/Vs$ at room temeperture. Another type of annealing of substrate-supported graphene devices is utilized by current-induced heating which is developed since the implementation of $H_2 - Ar$ environment in a cryostat is challenging. In this technique, huge amount of currents are passed through the device in order to heat the graphene up to $600°C$ [18].

However, these annealing techniques only remove the impurities above the graphene device, but not the disorders on the interface between Si substrate and the graphene. Later, physicists suspended the graphene layers by clamping them with metal contacts in order to achieve higher mobilities [19–22]. First, Bolotin et.al. fabricated a 4-probe suspended graphene device and achieve ultra-high mobility through current-induced annealing [21, 22] where their reported value for the graphene mobility was around $230.000\ cm^2/Vs$. But the problem with 4-probe goemtry, it is very hard to anneal the sample since the Hall probes act like an heat sink and it is almost unachievable to heat all the regions on the graphene with a uniform temperature. Ki et. al. showed that annealing one part of the sample makes dirty the other part and vice versa, and claimed that it is very hard to anneal the multi-terminal suspended devices with the contact geometry Bolotin et. al. used [23]. Similarly, Du et. al. reported 2-probe suspended graphene devices which were annealed at $H_2 - Ar$ environment and exhibited a similar mobility. Later using the quantum mobility formula which suggests that Shubnikov-de Haas oscillations start to appear when $\mu B \approx 1$, researches found that suspended graphene devices have mobilities exceeding $1.000.000\ cm^2/Vs$ [24].

In conclusion, suspended graphene devices can be cleaned with whether $H_2 - Ar$ annealing or current annealing, where former is harder to implement while the latter is more convenient to utilize. Moreover, 4-probe samples are harder to anneal due to the extra heat sinks introduced by the Hall probes. However, still the contacts may act as a heat sink in 2-probe geometry, since the current density needed to anneal the graphene ($\sim 1mA/\mu m$) [24] is too low to heat the Au/Cr contacts. Therefore, in the following sections, we investigate the effect of the contact designs and introduce a new design which allows us to heat up the contacts as well as the graphene in order to achieve uniform annealing.

4.2 Annealing with Split Contacts

As explained in last section, graphene annealing can be improved by passing high currents through the contacts for the overall heating of the sample in order to achieve cleaner samples. In this section, temperature simulations for various contact designs are introduced and the results are discussed.

4.2.1 Contact Designs and Temperature Simulations

This subsection serves to find an answer for how one can design the contacts for the most efficient annealing and optimum temperature for evaporating the impurities on the graphene to get a clean device. Several contact designs are discussed in terms of efficient graphene annealing with the Joule heating simulations of the metal contacts.

First of all, we have to justify the need for a split contact design for better annealing of the graphene. For a $1\mu m$ wide graphene, effective cleaning occurs when $\sim 1mA$ current passes through the graphene, which raises the temperature up to $600°C$. However, if the contacts are not split, this 1 mA current does not raise the temperature of the metal contacts up to such degrees and they act like a heat sink which prevents the dirt near the contacts to be evaporated. Figure 4.1 shows the temperature gradient on the contacts when $a)$ 1 mA and $b)$ 40 mA current pass through the metal. In the former case, contacts heat only up to $10°K$, while in the latter, contacts can reach up to $400°K$ which is enough for the contacts not to act as a heat sink.

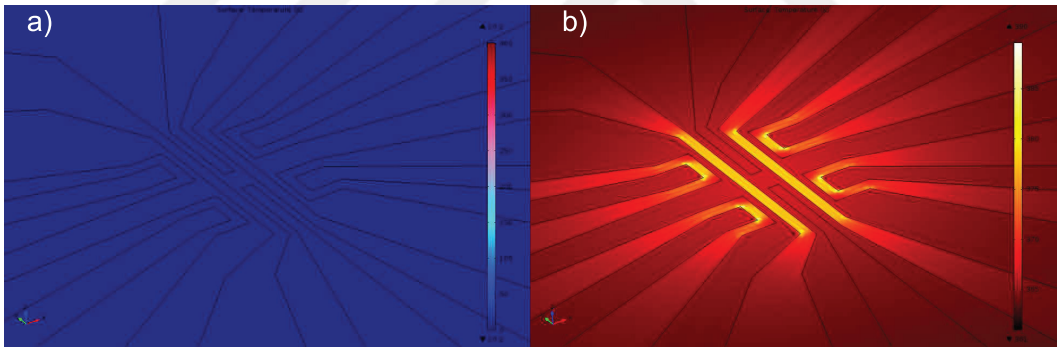

Figure 4.1: a) When $1mA$ passes through the contacts, metal heats only up to $10°K$ b) $40mA$ passing through the contacts. Metal heats up to $400°K$.

Next, we consider different designs in terms of the ability to reach high temperatures and the sustainability of the contacts during the annealing. At such high temperatures, contacts may be lost because of the excessive heating of some of the regions on the contact, which can be eliminated with an optimized design. From the simulations, we deduce that sharp corners on the design may raise the temperature on that spots more than the part that touches to the graphene. Therefore, it is essential to avoid sharp corners and narrow regions in the contact design, which may increase the chance of the survival of the contacts during current annealing. In Figure 4.2, two different designs with sharp corners and smooth corners are compared in terms of temperature gradients. It is obvious that

sharp regions have more temperature than the parts which touch to the graphene in Figure 4.2a. This may lead the contacts to be damaged quickly than the one which has smooth corners as shown in Figure 4.2b, where smooth turns are not heated as much as the contact regions to the graphene.

One last consideration is the width of the contacts touching to the graphene. Narrower contacts can ramp up to higher temperatures, but it also may lead the collapse of the graphene while HF etching. On the other hand, wider contacts need higher currents to reach the desired temperature which may also damage the device, and therefore, reduce the sustainability of the graphene device. Our experiences show that graphene contacts with width $1 - 2\mu m$ are ideal for graphene annealing. These contacts reach to the desired temperatures with currents around $30 - 40mA$.

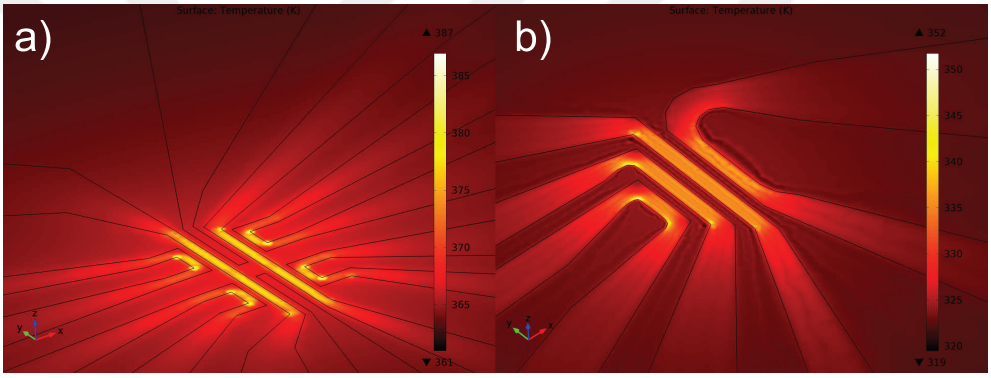

Figure 4.2: a) Sharp corners create hot spots which may damage the contacts during the annealing. b) If the corners smoothed in the design, hot spots disappear and metal contacts become more sustainable.

4.2.2 Automatic Annealing Software

In this subsection, we explain the annealing procedure utilized using a computer software which eases the annealing process and helps to prevent unwanted device damages. Since in our technique, we must raise the current passing through the split contacts up to 40 mA, we should do it step by step in order to prevent graphene damage. This software first increases the current on the contacts by the amount set on the program while keeping a constant low current passing through the graphene in order to monitor the changes in the resistance during the process.

In Figure 4.3, electrical connections to the graphene device is shown. Here I_{probe} is the current which user wants to reach for the heating of the contacts, and $I_{graphene}$ is the current which passes during the contacts are ramping up to the desired current

value. I_{probe} is slowly increased with the steps set by the user. When the program is started, first I_1 is set to $\Delta I + I_{graphene}$, where ΔI is the current increment for the contact current. Then immediately after, I_2 is set to $-\Delta I$. Therefore in that short time between the setting of I_1 and I_2, $\Delta I + I_{graphene}$ amount of current passes through the graphene. But, since ΔI is usually set to $\sim 50\mu A$, no harm is given to the graphene. Then, same happens to current I_3 which is set to ΔI again. But this time, since the other end of the contact is connected to the drain (0 V), there is no need to pass a negative current from the end which is connected to the drain. This process continues $I_{probe}/\Delta I$ times, until the current passing through the contacts reaches to I_{probe}. Then, program changes it state: Now only I_1 current becomes controllable. Since contacts reached to the desired value, we slowly increase the current passing through the graphene, which is controlled by $I_1 = I_{probe} + I_{graphene}$, while monitoring the change in the graphene resistance, until graphene finally heats up, and hopefully shows a significant change in its resistance which implies that some dirt on it has just evaporated.

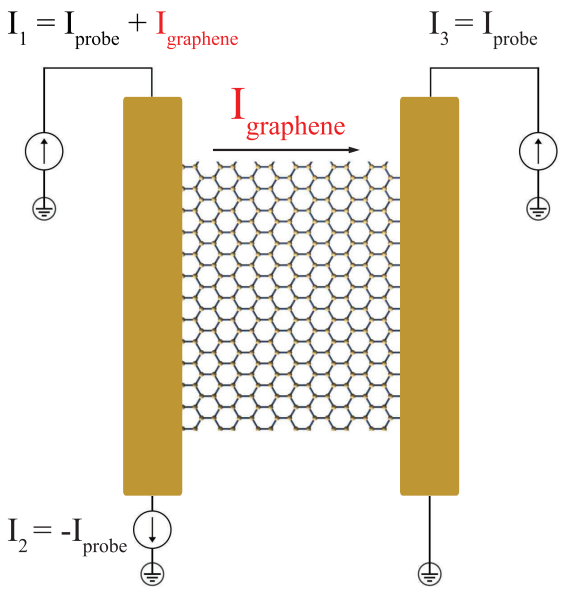

Figure 4.3: Electrical setup for current annealing.

After observing a significant and sudden change in the graphene resistance, user presses the "Stop The Annealing" button and program again changes its state: Now, first $I_{graphene}$ comes back to its initial low current step by step, then same happens for I_{probe} which is slowly lowered with the same increment/decrement step ΔI. Program also embodies a quick gate-sweep program which allows the user to sweep the gate of the device

in order to check if there is a remarkable change in the quality of the graphene. If, it is still not in a good condition, then user repeats this process until catching a high-mobility device. A flowchart and the user interface of the software is shown in Figure 4.4a and 4.4b.

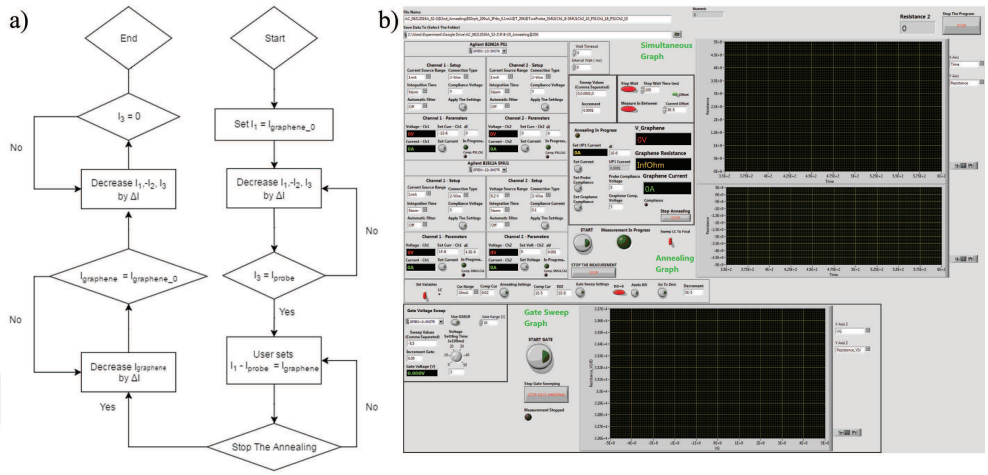

Figure 4.4: a) Flowchart of the annealing software. b) User interface of the software.

Chapter 5

REALIZATION OF SUSPENDED GRAPHENE DEVICES

In this chapter, we review the fabrication process described in Chapter 3 together with the applications of these techniques on real devices. Many devices fabricated during this work, but here, only four of them are presented which are different from the samples presented in Chapter 3. Furthermore, various technical difficulties encountered during the fabrication and their possible solutions are discussed. Two of these devices are not suspended due to the etching problem mentioned in Chapter 3, and labeled as U1 and U2. The other two are successfully etched after solving the problem and labeled as S1 and S2.

After the fabrication section, results of the current annealing utilized on successfully fabricated samples are shared, and again, its technical difficulties are discussed with possible solutions.

Finally, transport experiments of the suspended graphene devices successfully survived from the previous two procedures are presented, and the results obtained after the experiments are discussed.

5.1 Fabrication of the Suspended Devices

As described in Chapter 3, we obtain the graphene by mechanical exfoliation, characterized them with Raman spectroscopy and fabricated the devices with E-Beam lithography and wet etching.

Graphenes in U1 and U2 are exfoliated on a silicon substrate which is cleaned only by piranha solution as mentioned in Chapter 3. Graphenes are confirmed to be monolayers with Raman spectroscopy and the designs are made as seen in Figure 5.1 and Figure 5.2

for U1 and U2, respectively.

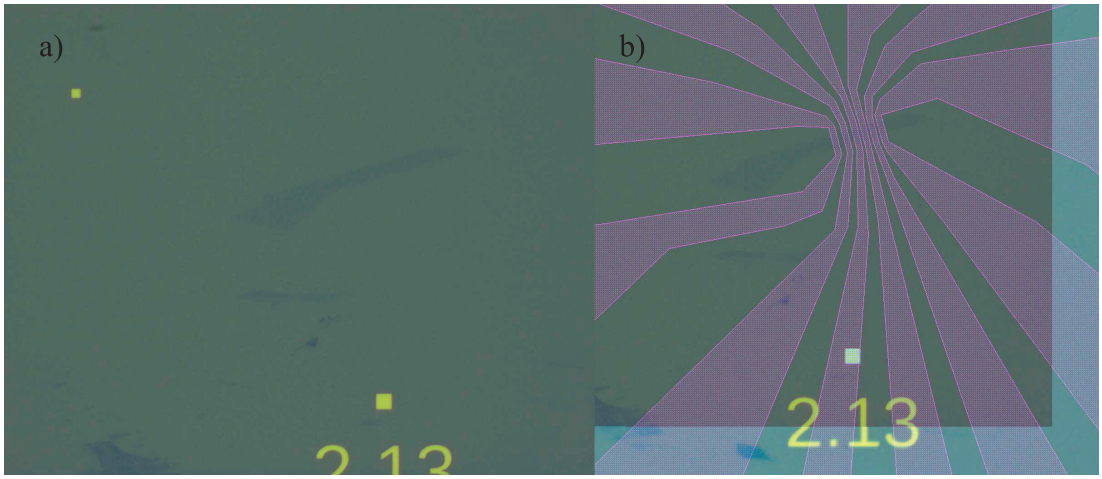

Figure 5.1: a) Exfoliated graphene in U1 without any process. b) Contact design of U1.

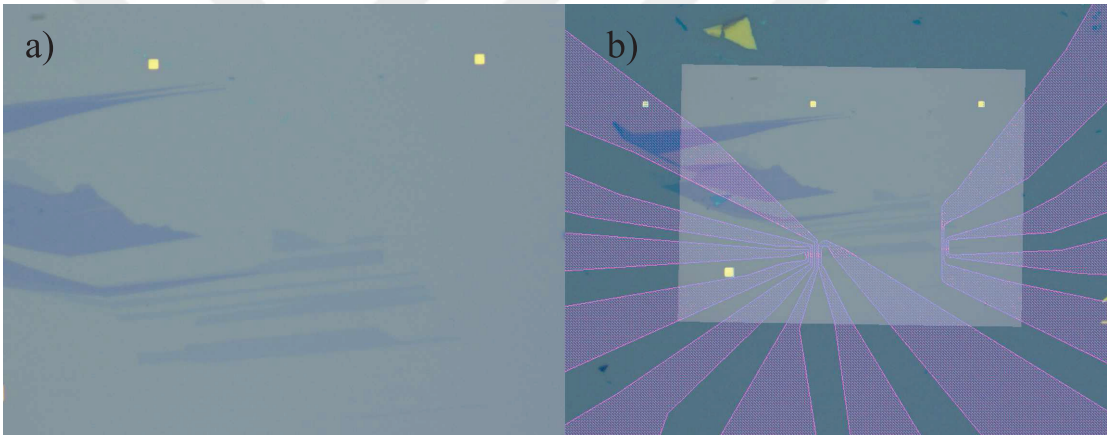

Figure 5.2: a) Exfoliated graphene in U2 without any process. b) Contact design of U2.

Then, samples are coated with MMA EL 11 and 950 PMMA A2 with 450 nm and 100 nm, respectively. Using these designs, samples are e-beam exposed and developed with 3:1 MIBK-IPA. Resulting patterns are shown in Figure 5.3a and Figure 5.3b for U1 and U2, respectively.

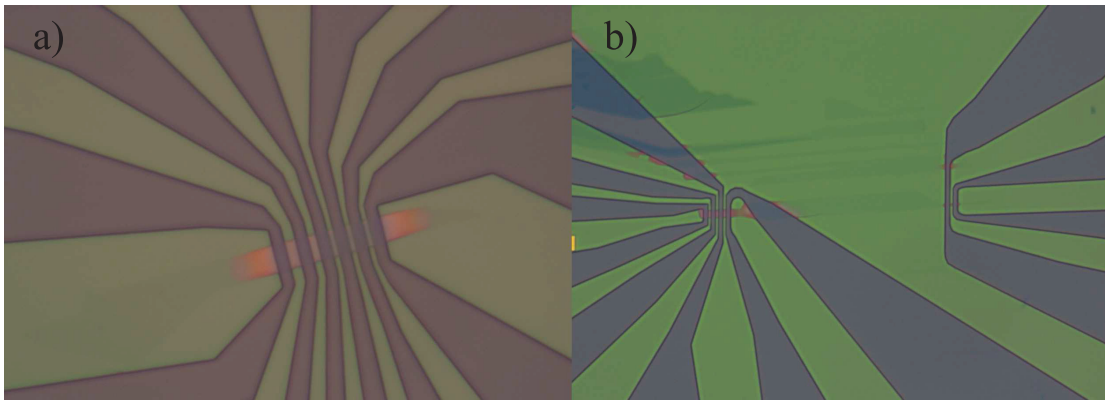

Figure 5.3: a) U1 after E-Beam lithography and developing. b) U2 after E-Beam lithography and developing.

After this step, we put them into the vacuum chamber and wait for the vacuum to reach $\sim 10^{-7}\,Torr$ pressure. Then, we evaporate 2 nm Cr and 100 nm Au for the metal contacts. After the evaporation, we leave the samples under acetone for several hours to lift-off the metal films coated on the PMMA resist. Figure 5.4a and 5.4b show the pictures of U1 and U2, respectively, after lift-off process.

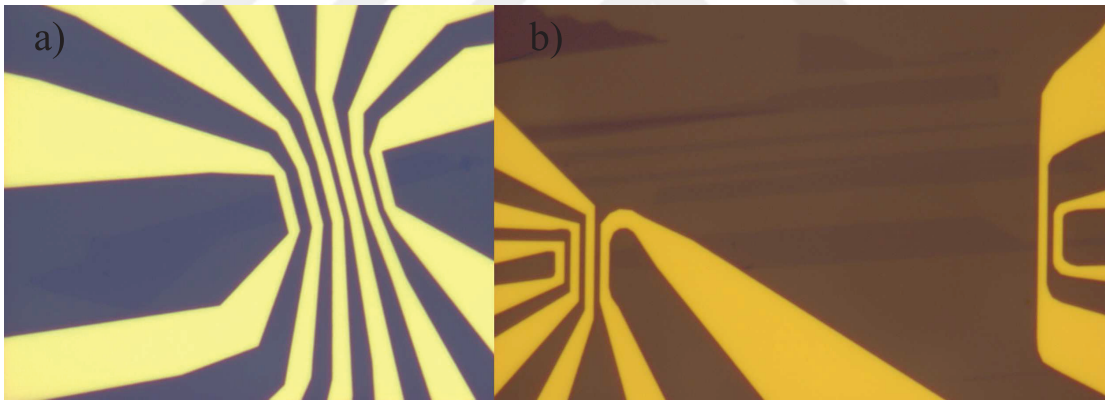

Figure 5.4: a) U1 after lift-off of the metal. b) U2 after lift-off of the metal.

Finally, we etch the samples with 7:1 BOE. Resulting device images are shown in Figure 5.5a and 5.5b for U1 and U2, respectively. As we mentioned above, these etchings were not successful. In order to understand the reason clearly, we took their Scanning Electron Microscope (SEM) images by tilting the samples by 80°. SEM images of U1 and U2 are shown in Figure 5.6 and 5.7, respectively. From these images, we can see that SiO_x is only partially etched and then graphene collapses which prevents the BOE enter further into the graphene to etch the remaining oxide. It is known that, when the sample is first dipped into the etchant, BOE quickly enters underneath the graphene in the interface and starts a homogeneous etching. But it seems that in our samples, U1 and U2, BOE

could not enter in the interface and left the devices collapsed. This information suggests us that the substrate was initially dirty or there was another surface related problem and piranha was not able to clean the surface, completely. Then, we tried RIE cleaning on the substrates from the same set, and repeat the whole procedure starting from graphene exfoliation.

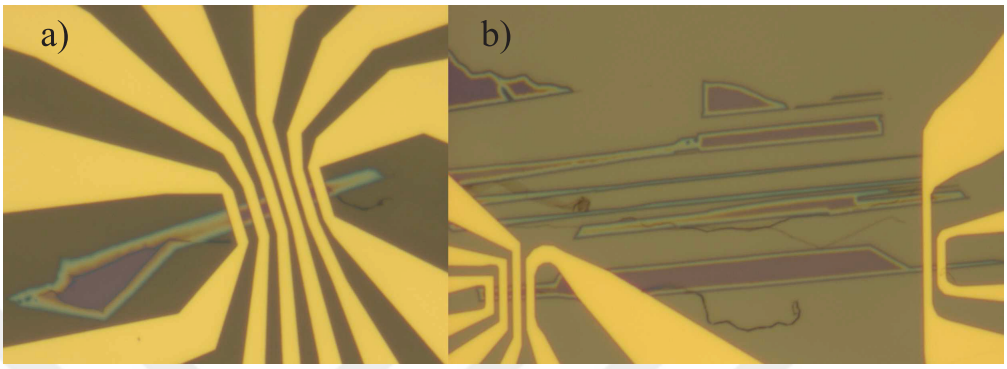

Figure 5.5: a) U1 after BOE etching. Having a graphene contrast between the metal probes implies that it is not etched completely. b) U2 after BOE etching. Having a graphene contrast between the metal probes implies that it is not etched completely.

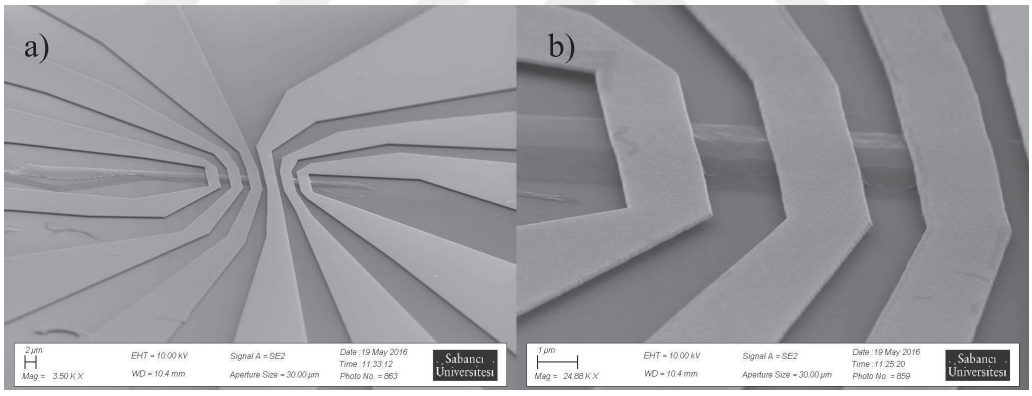

Figure 5.6: a) An overview of U1 under SEM. b) A closer look on the unsuspended graphene regions.

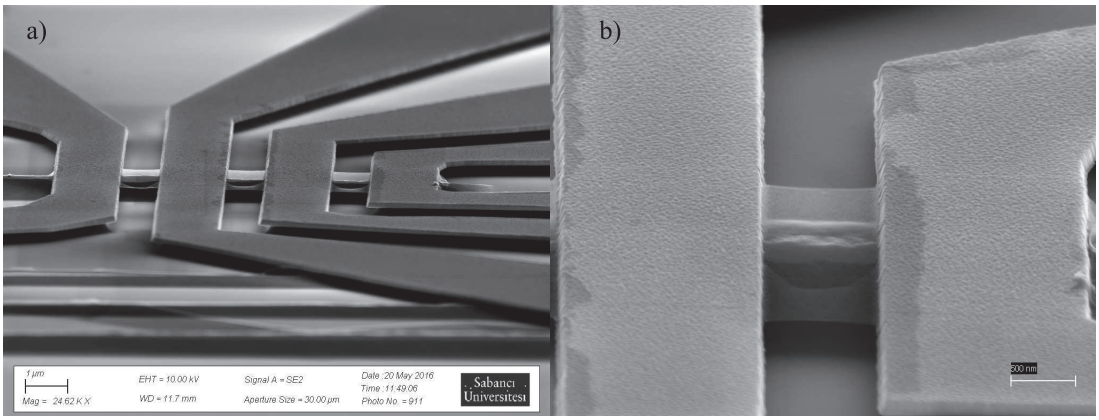

Figure 5.7: a) An overview of U2 under SEM. b) A closer look on the unsuspended graphene regions.

After cleaning the samples with oxygen plasma using an Oxford Instruments RIE system, we fabricate S1 and S2, which are successfully etched and suspended. Graphenes and the contact designs made for S1 and S2 are seen in Figure 5.8 and Figure 5.9 for S1 and S2, respectively.

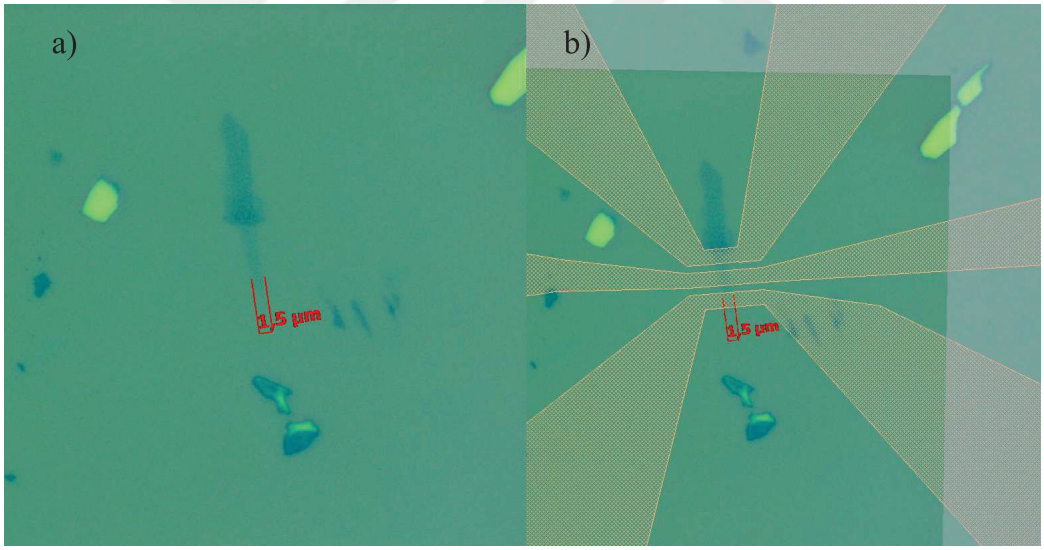

Figure 5.8: a) Exfoliated graphene in S1 without any process. b) Contact design of S1.

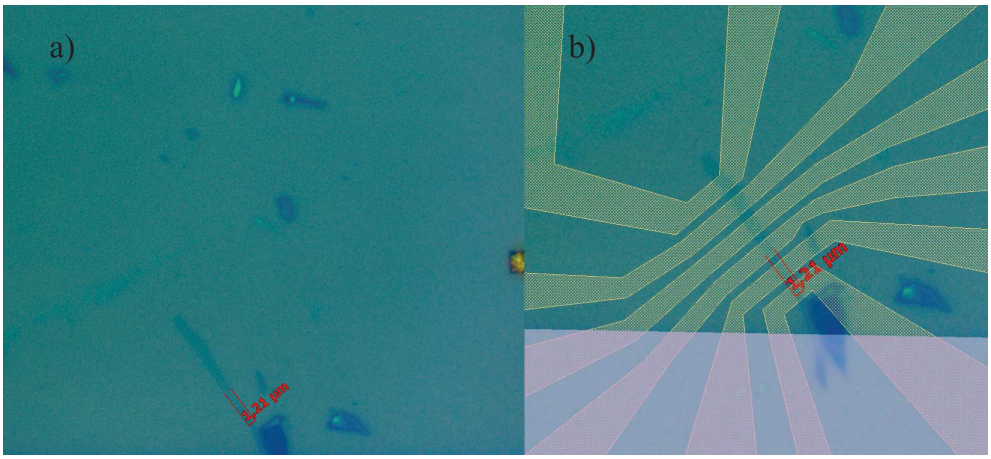

Figure 5.9: a) Exfoliated graphene in S2 without any process. b) Contact design of S2.

Then, we utilize the same E-Beam procedure by coating the resists and developing the samples after exposure. Patterns are shown in Figure 5.10a and Figure 5.10b for S1 and S2, respectively. After the developing of the samples, we evaporate 2 nm Cr and 100 nm Au on the devices, and utilize lift-off. Figure 5.11a and 5.11b show the pictures of S1 and S2, respectively, after lift-off process.

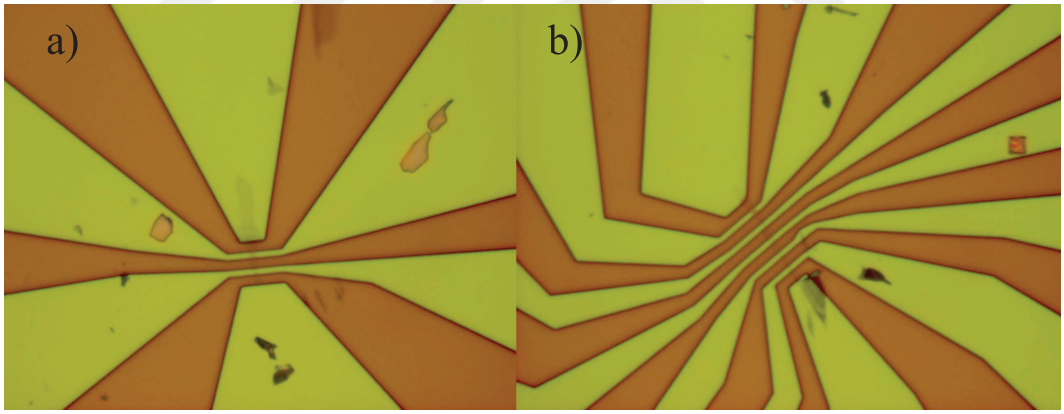

Figure 5.10: a) S1 after E-Beam lithography and developing. b) S2 after E-Beam lithography and developing.

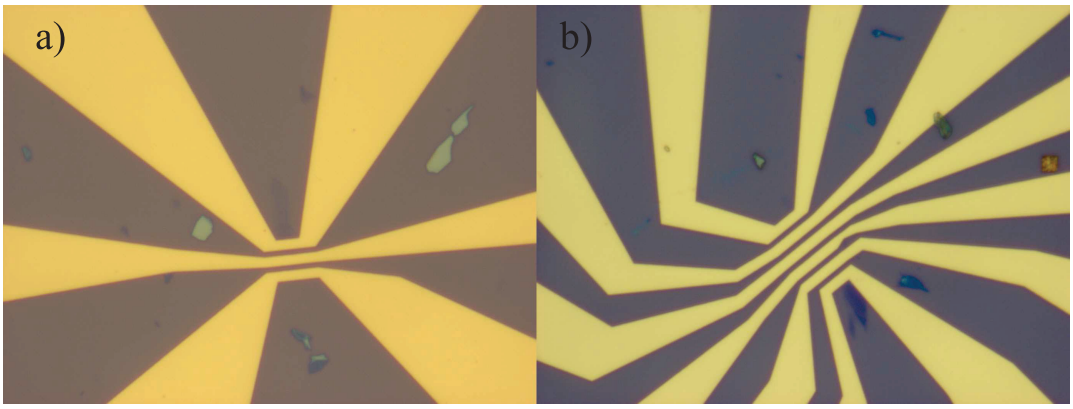

Figure 5.11: a) S1 after lift-off of the metal. b) S2 after lift-off of the metal.

Finally, we etch the samples with 7:1 BOE etchant the results are affirmative. Figure 5.12a and 5.12b show the images of S1 and S2 after SiO_x etching, respectively.

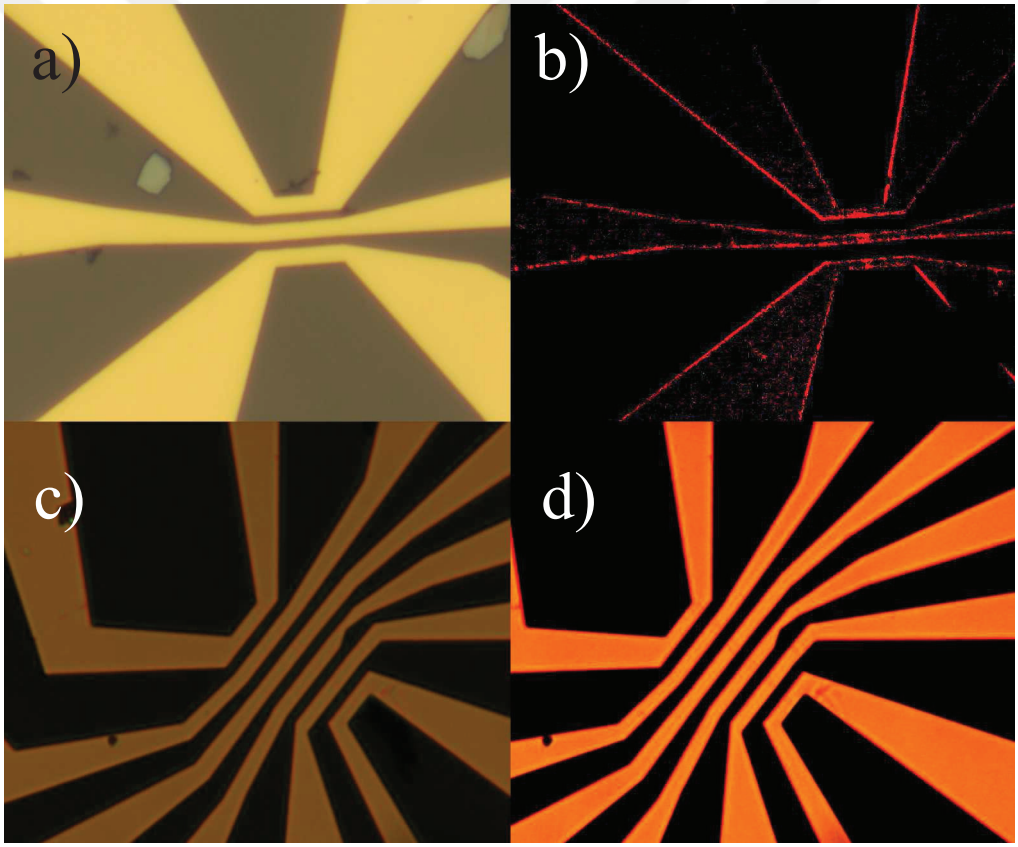

Figure 5.12: a,b) S1 after BOE etching. Graphene cannot be seen in normal optical image but it can be seen after changing the contrast. c,d) S2 after BOE etching. Graphene cannot be seen in normal optical image but it can be seen after changing the contrast.

These results conclude this section by remarking that oxygen plasma is a must before exfoliating the graphene on SiO_x substrate.

5.2 Current Annealing

In this section, we present our results obtained from the devices we fabricated as described in Chapter 3, and annealed as explained Chapter 4. Here, we present the annealing of S2 which was unsuccessful and another sample S3 which was successful.

S2 is wire bonded and loaded into an Oxford Triton 400 10mK dilution refrigerator at room temperature. Then, we start cooldown of the system down to 10 K in which temperature we anneal our sample. Using a Stanford Research Systems SR830 DSP lock-in amplifier, we measure the device resistance versus temperature during cooldown. Figure 5.13 shows the resistance changes from 300 K to 10 K with respect to gate voltage. As it can be seen from this figure, graphene resistance does not show Dirac-like behavior and any significant change with temperature.

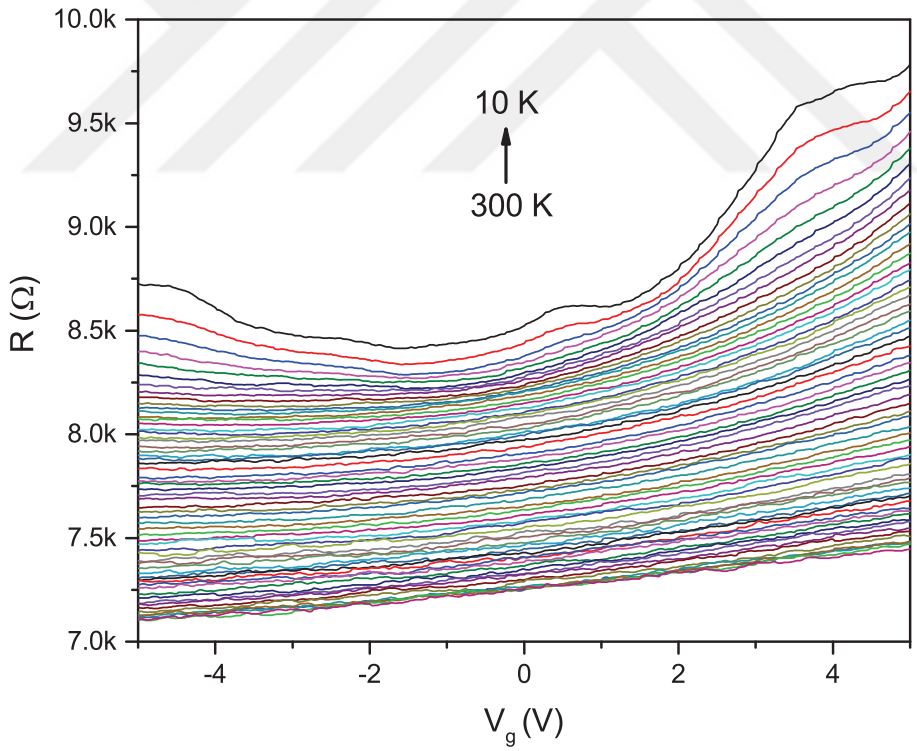

Figure 5.13: Gate dependence of S2 resistance with varying temperature, from 300 K to 10 K.

When system reaches to 10 K, we start annealing procedure explained in Chapter 4. We have three suspended two-probe samples in this device and present the annealing

results of each of them. We call these separate two-probe devices D1, D2 and D3. These devices correspond to the graphenes between $3^{rd} - 6^{th}$, $6^{th} - 7^{th}$ and $7^{th} - 8^{th}$ probes of the chip.

In Figure 5.14, we show the resistance change of D1 with respect to gate voltage. Black line is the gate sweep before annealing which shows that the sample is very dirty and there is no observable Dirac point. In the first annealing of graphene, we catch the Dirac point around zero gate voltage with 600 μA current passing through the graphene and 1 mA current passing through the probes, which does not heat it as shown in Chapter 4. After second and third annealing, which are done in 600 μA graphene current as well, we do not see any remarkable difference. When we try to pass 620 μA current through the graphene, it is burned due to excessive heating. In this sample, contact resistance is also very high around $10k\Omega$ as opposed to expected values around $1 - 2k\Omega$. High contact resistances are usually a result of dirt on the graphene existing before putting the contacts, which are probably due to the PMMA residues. In order to solve the contact problem, we should whether develop the sample more in order to resolve the residues after E-Beam, or dip the sample into an acid solution, which is usually HCl, in order to remove existing dirt on the graphene during the fabrication.

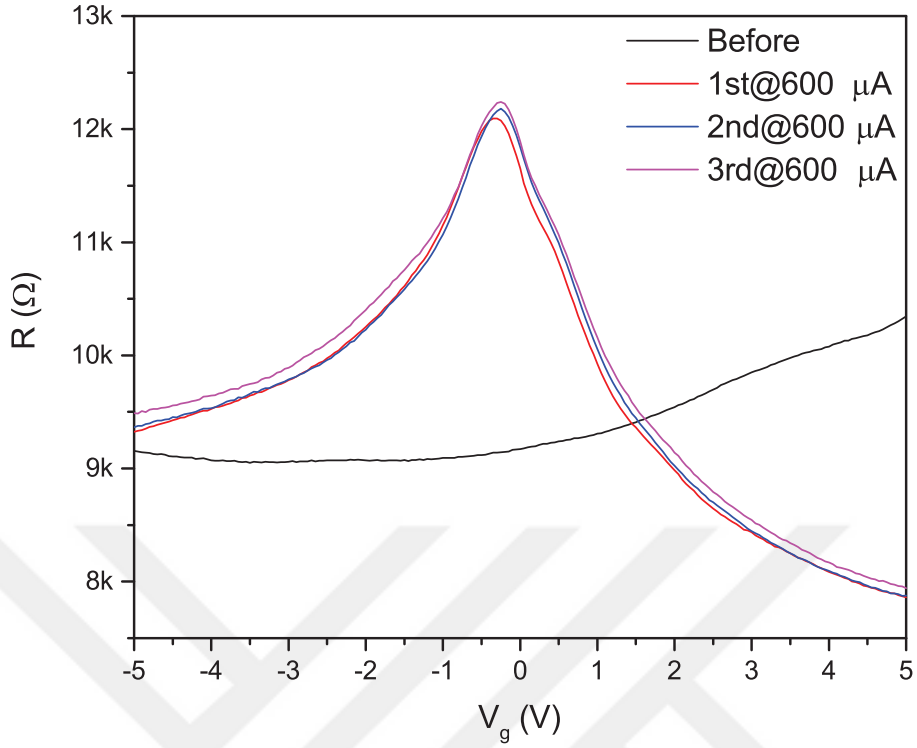

Figure 5.14: Gate sweeps of D1 after each graphene annealing. Black, red, blue and pink curves correspond to the gate sweeps before, 1^{st}, 2^{nd} and 3^{rd} annealing, respectively.

Current annealing results of the device D2 is shown in Figure 5.15 where we have four annealing steps. Black line shows the gate sweep before the annealing. As can be seen from the graph, its resistance values are much higher than the resistance of D1. This is again because of the contact problems. Most probably, there is a chronic dirtiness problem in this device which stems from the fabrication process. Yet, we tried annealing on this device, and the red line shows the result after the 1^{st} annealing with $110\mu A$ graphene current and 1 mA probe current, where we catch the Dirac point. This result confirms that the device is indeed suspended and its resistance changes by 10 $k\Omega$ which is an indicator about the graphene's high quality. Unfortunately, its contact resistance is too high and after each annealing, it gets higher and higher. This is most probably due to the damage given to the contact-graphene interface during the annealing, which is very loose in our case because of the PMMA residues sitting on the interface. In 5^{th} annealing with 150 μA graphene current, we lose the sample due to the excessive heating around the graphene-metal interface which becomes highly resistive.

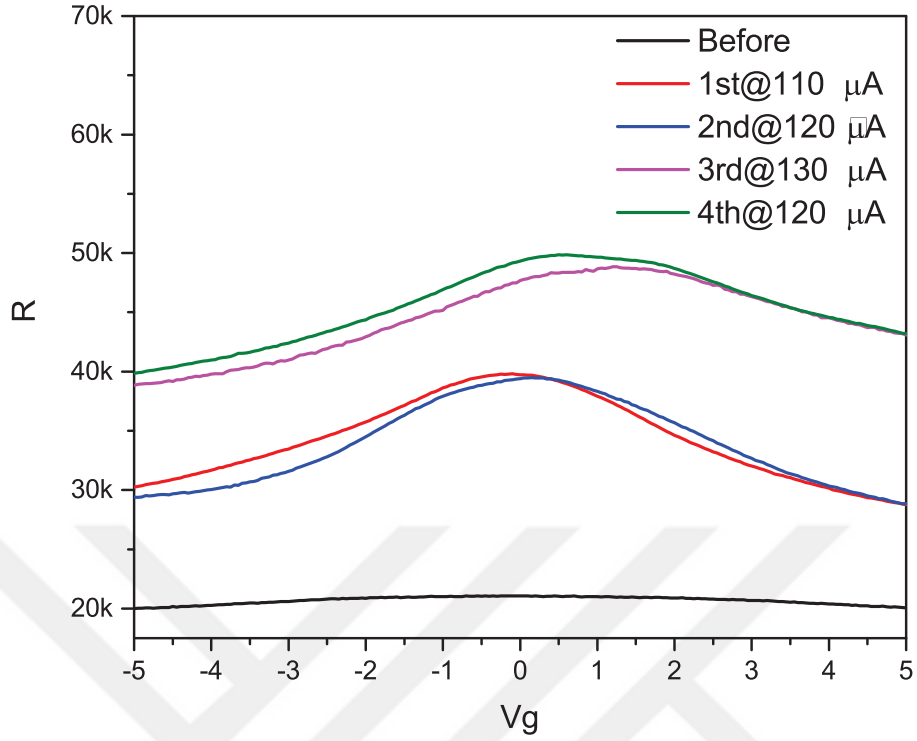

Figure 5.15: Gate sweeps of D2 after each graphene annealing. Black, red, blue, purple and green curves correspond to the gate sweeps before, 1^{st}, 2^{nd}, 3^{rd} and 4^{th} annealing, respectively.

Finally, we present the last device on this chip, D3. Its gate sweep curves are shown in Figure 5.16 where we again have a very high device resistance around $20k\Omega$. Cyan curve shows the gate sweep before annealing and the black curve shows the gate sweep after first annealing where graphene current is 300 μA and probe current is 1 mA. In the gate sweep after first annealing, we observe a Dirac-like shape but it is still not we want. In second annealing shown with red curve where graphene current is 350 μA and probe current is 1 mA, we get a nice Dirac peak and the resistance increases by 10 $k\Omega$. In the other annealing until the 10^{th} annealing, we do not observe a remarkable change. In 10^{th} annealing where graphene current is 50 μA but probe current is 40 mA which we show that it heats the probes. Although we pass a small current from graphene, sweep shape becomes more Dirac-like and the resistance in the shoulders are dropped. This is a manifestation of the importance of contact heating which we claim in this thesis. In 13 th annealing we observe a better shape where the Dirac point is exactly on 0 gate voltage which indicates that the electron-hole puddles and other impurities are completely cleaned

which shifts the Dirac peak away from 0. In this annealing, we pass 310 μA current from graphene and 55 mA from the probes. But still our contact resistance is so high which obscures the observation of quantum Hall steps in graphene which are 4.3 $k\Omega$, 12.9 $k\Omega$ and 25.8 $k\Omega$ for the filling factors ν 6, 2 and 1 respectively. Hoping the reduction of the contact resistance, we try further annealing but in 14 th annealing it jumps to around 100 $k\Omega$ and in the 16 th annealing it is burned. However, this device is a good evidence that annealing the probes by split contacts improves the quality of the graphene. If these devices were low contact resistance which is a matter of successful fabrication, then we would obtain a ultra-high mobility suspended graphene device.

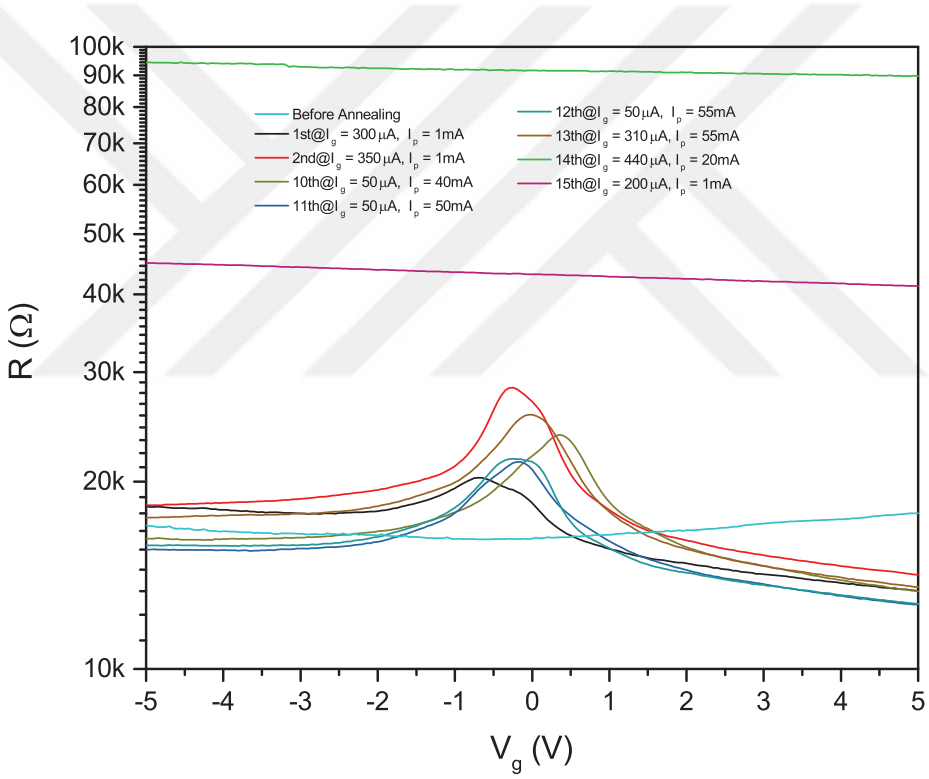

Figure 5.16: Gate sweeps of D3 after each graphene annealing.

Next sample we present here is the current annealing results of S3 which is fabricated with the same sequence and successfully suspended. In Figure 5.17a, optical picture of the graphene device is shown after the suspension. Figure 5.18b shows the gate sweep curves of the device at 200 K, 30 K and 20 mK before annealing, and after the 1 st annealing where the graphene current is 1.1 mA. This device shows a Dirac-like behavior even at high temperatures and before any heat treatment. Moreover, its resistance is around $1k\Omega$

which indicates that it has very low contact resistance and clean metal-graphene interface. This results show us that every step of the graphene device fabrication is very important to ultimately reach a working sample.

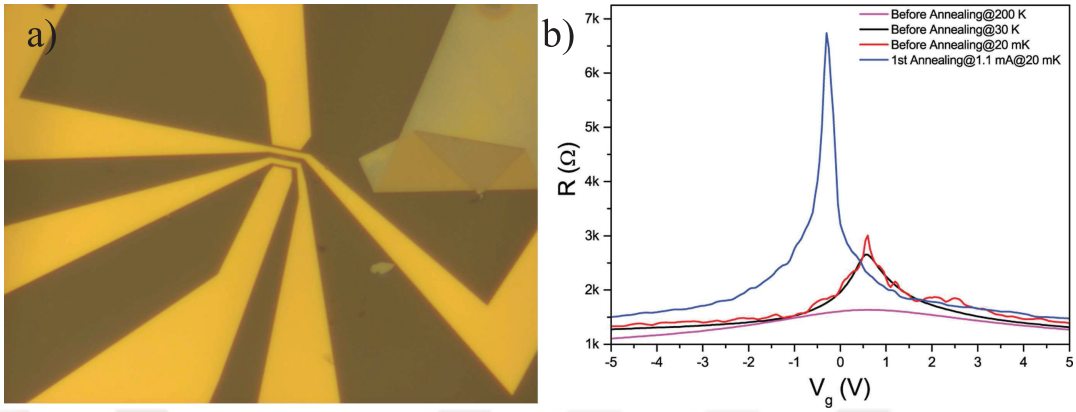

Figure 5.17: a) Optical image of the device S3 after BOE etching. b) Gate sweeps of S3 before and after annealing. Pink, black and red curves show the gate sweeps at 200 K, 30 K and 20 mK, respectively. Blue line shows the gate sweep and the improvement in the graphene quality after the first annealing.

5.3 Transport Experiments after Current Annealing

In this section, we present the electrical transport experiments carried out on the device S3 presented in the last section.

Figure 5.18a shows the quantum mobility calculation in order to extract the carrier mobility of the suspended device for determining its quality. In this calculation, as explained in Chapter 4, we look at the magnetic field in which the Dirac peak splits into two in order to form the first Hall plateaus $\nu = \pm 2$ and using the relation $\mu_Q B_q \sim 1$, we obtain the quantum mobility of this device as $\mu Q \approx 2 \times 10^6 cm^2 V s^{-1}$ which is, compared to literature, described as ultra-high mobility [24]. Figure 5.18b shows the quantum Hall effect observed in our device where the quantum Hall sequence $\nu = \pm 2, \pm 6$ is easily seen. Furthermore, we observe the signature of $\nu = \pm 1$ as well, which is whether a result of valley symmetry breaking or strongly correlated electron interactions which breaks the chiral symmetry in graphene [25]. This justifies that we can observe interesting many-body physics in graphene by fabrication ultra-clean graphene devices, which is our driving purpose as mentioned at the beginning of this thesis. By utilizing our split contact design and current annealing technique, we are able to fabricate ultra-high mobility samples which can show strongly correlated phenomena.

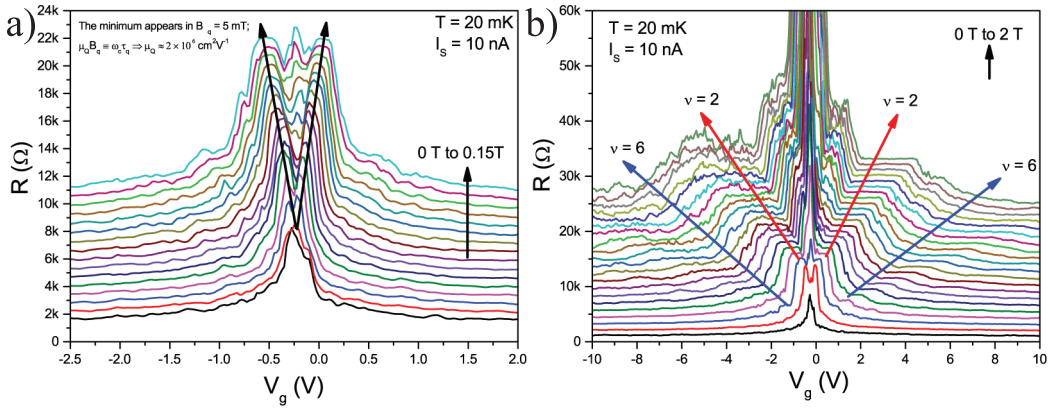

Figure 5.18: a) Quantum mobility of the sample S3 extracted from the magnetic field where Dirac peak starts to split into two to form $\nu = \pm 2$ plateaus. b) Quantum Hall Effect measured in sample S3. Filling factors $\nu = \pm 2, \pm 6$ are drawn in the graph.

Chapter 6

CONCLUSION

In this thesis, we have studied the fabrication of an ultra-clean and high-mobility suspended monolayer graphene which can be further investigated through electrical measurements in order to reveal the interesting many-body strongly correlated condensed matter systems.

We first started with justifying the need of graphene research for the fundamental physics by claiming that graphene with its relativistic Dirac excitations is very special in terms of the study of strongly correlated electron systems and high-speed electronics, as well. Its impressive mechanical and chemical properties make it a good candidate for technological applications such as gas sensors or nano-electro-mechanical-systems (NEMS). Therefore, a better understanding of graphene may enable us to reach previously unavailable high technologies as well as the fundamental physics.

In the second chapter, we investigated the electronic transport properties of graphene and review some concepts such as classical and quantum Hall effect. We derived the graphene Hamiltonian and its energy-momentum dispersion relation by using tight-binding approach. Then, both Hall effects, classical and quantum, are reviewed in order to understand the transport properties of graphene under magnetic field. Finally, we explained the anomalous Hall sequence of graphene, which turns out to be a result of its relativistic nature.

In the third chapter, we introduced the fabrication techniques we use during our device preparation. We divided this chapter into two and study the preparation of graphene layers via mechanical cleavage and clean-room process consisting of contact design, E-Beam lithography and substrate etching, in depth.

In the fourth chapter, we discussed the need of suspended graphene devices for reaching high-quality devices and explain the current annealing technique for suspended graphene,

which is a must in order to achieve our purposes. Rather than direct annealing of graphene which is how graphene annealing is done in literature, we suggested to heat the contacts as well in order to clean the graphene device thoroughly. We present our simulation results of our contact designs and tried to figure out the optimum probe designs and current densities needed to pass through the contacts for effectively anneal our samples. Then a software which is developed to utilize graphene annealing without damaging the sample and to monitor every change in the graphene transport while annealing.

In the final chapter, we presented our real devices fabricated in the clean-room and measured in the lab. We first review the fabrication process of each device as presented in the Chapter 3. Then we shared four devices with their pictures during the fabrication and some complications which are arisen during the fabrication. We tried to solve these complications and discussed the possible reasons. Then, we showed the data of annealing of each device. Finally, we presented the transport measurements of a successfully fabricated, suspended and annealed sample and showed that we can really achieve ultra-high quality suspended graphene devices with these techniques.

Bibliography

[1] A. H. Castro Neto, F. Guinea, N. M. R. Peres, K. S. Novoselov, and A. K. Geim, "The electronic properties of graphene," *Rev. Mod. Phys.*, vol. 81, pp. 109–162, Jan 2009.

[2] R. Kundu, "Tight-binding parameters for graphene," *Modern Physics Letters B*, vol. 25, no. 03, pp. 163–173, 2011, http://www.worldscientific.com/doi/pdf/10.1142/S0217984911025663.

[3] K. v. Klitzing, G. Dorda, and M. Pepper, "New method for high-accuracy determination of the fine-structure constant based on quantized hall resistance," *Phys. Rev. Lett.*, vol. 45, pp. 494–497, Aug 1980.

[4] K. S. Novoselov, A. K. Geim, S. V. Morozov, D. Jiang, M. I. Katsnelson, I. V. Grigorieva, S. V. Dubonos, and A. A. Firsov, "Two-dimensional gas of massless dirac fermions in graphene," *Nature*, vol. 438, pp. 197–200, Nov 2005.

[5] K. S. Novoselov, A. K. Geim, S. V. Morozov, D. Jiang, Y. Zhang, S. V. Dubonos, I. V. Grigorieva, and A. A. Firsov, "Electric field effect in atomically thin carbon films," *Science*, vol. 306, no. 5696, pp. 666–669, 2004, http://science.sciencemag.org/content/306/5696/666.full.pdf.

[6] A. K. Geim and K. S. Novoselov, "The rise of graphene," *Nat Mater*, vol. 6, pp. 183–191, Mar 2007.

[7] D. A. Abanin, S. V. Morozov, L. A. Ponomarenko, R. V. Gorbachev, A. S. Mayorov, M. I. Katsnelson, K. Watanabe, T. Taniguchi, K. S. Novoselov, L. S. Levitov, and A. K. Geim, "Giant nonlocality near the dirac point in graphene," *Science*, vol. 332, no. 6027, pp. 328–330, 2011, http://science.sciencemag.org/content/332/6027/328.full.pdf.

[8] D. A. Bandurin, I. Torre, R. K. Kumar, M. Ben Shalom, A. Tomadin, A. Principi, G. H. Auton, E. Khestanova, K. S. Novoselov, I. V. Grigorieva, L. A. Ponomarenko, A. K. Geim, and M. Polini, "Negative local resistance caused by viscous electron backflow in graphene," *Science*, 2016, http://science.sciencemag.org/content/early/2016/02/10/science.aad0201.full.pdf.

[9] J. Crossno, J. K. Shi, K. Wang, X. Liu, A. Harzheim, A. Lucas, S. Sachdev, P. Kim, T. Taniguchi, K. Watanabe, T. A. Ohki, and K. C. Fong, "Observation of the dirac fluid and the breakdown of the wiedemann-franz law in graphene," *Science*, 2016, http://science.sciencemag.org/content/early/2016/02/10/science.aad0343.full.pdf.

[10] P. R. Wallace, "The band theory of graphite," *Phys. Rev.*, vol. 71, pp. 622–634, May 1947.

[11] D. Tong, "The quantum hall effect lectures," 2016.

[12] V. P. Gusynin and S. G. Sharapov, "Unconventional integer quantum hall effect in graphene," *Phys. Rev. Lett.*, vol. 95, p. 146801, Sep 2005.

[13] D. Gardiner, P. Graves, and H. Bowley, *Practical Raman spectroscopy*. Springer-Verlag, 1989.

[14] L. Malard, M. Pimenta, G. Dresselhaus, and M. Dresselhaus, "Raman spectroscopy in graphene," *Physics Reports*, vol. 473, no. 5–6, pp. 51 – 87, 2009.

[15] Cornell, "Spie handbook of microlithography, micromachining and microfabrication," 2016. [Online; accessed 8-Temmuz-2016].

[16] R. R. Nair, P. Blake, A. N. Grigorenko, K. S. Novoselov, T. J. Booth, T. Stauber, N. M. R. Peres, and A. K. Geim, "Fine structure constant defines visual transparency of graphene," *Science*, vol. 320, no. 5881, pp. 1308–1308, 2008, http://science.sciencemag.org/content/320/5881/1308.full.pdf.

[17] S. V. Morozov, K. S. Novoselov, M. I. Katsnelson, F. Schedin, D. C. Elias, J. A. Jaszczak, and A. K. Geim, "Giant intrinsic carrier mobilities in graphene and its bilayer," *Phys. Rev. Lett.*, vol. 100, p. 016602, Jan 2008.

[18] J. Moser, A. Barreiro, and A. Bachtold, "Current-induced cleaning of graphene," *Applied Physics Letters*, vol. 91, no. 16, 2007.

[19] J. C. Meyer, A. K. Geim, M. I. Katsnelson, K. S. Novoselov, T. J. Booth, and S. Roth, "The structure of suspended graphene sheets," *Nature*, vol. 446, pp. 60–63, Mar 2007.

[20] X. Du, I. Skachko, A. Barker, and E. Y. Andrei, "Approaching ballistic transport in suspended graphene," *Nat Nano*, vol. 3, pp. 491–495, Aug 2008.

[21] K. Bolotin, K. Sikes, Z. Jiang, M. Klima, G. Fudenberg, J. Hone, P. Kim, and H. Stormer, "Ultrahigh electron mobility in suspended graphene," *Solid State Communications*, vol. 146, no. 9–10, pp. 351 – 355, 2008.

[22] K. I. Bolotin, K. J. Sikes, J. Hone, H. L. Stormer, and P. Kim, "Temperature-dependent transport in suspended graphene," *Phys. Rev. Lett.*, vol. 101, p. 096802, Aug 2008.

[23] D.-K. Ki and A. F. Morpurgo, "High-quality multiterminal suspended graphene devices," *Nano Letters*, vol. 13, no. 11, pp. 5165–5170, 2013, http://dx.doi.org/10.1021/nl402462q. PMID: 24080018.

[24] D. C. Elias, R. V. Gorbachev, A. S. Mayorov, S. V. Morozov, A. A. Zhukov, P. Blake, L. A. Ponomarenko, I. V. Grigorieva, K. S. Novoselov, F. Guinea, and A. K. Geim, "Dirac cones reshaped by interaction effects in suspended graphene," *Nat Phys*, vol. 7, pp. 701–704, Sep 2011.

[25] B. Roy, M. P. Kennett, and S. Das Sarma, "Chiral symmetry breaking and the quantum hall effect in monolayer graphene," *Phys. Rev. B*, vol. 90, p. 201409, Nov 2014.